LAWRENCE
LIVERMORE
NATIONAL
LABORATORY

LLNL-JRNL-659268

Large-Eddy and Unsteady RANS Simulations of a Shock-Accelerated Heavy Gas Cylinder

B. E. Morgan, J. A. Greenough

August 26, 2014

Shock Waves

Disclaimer

Shock Waves manuscript No.
(will be inserted by the editor)

Large-Eddy and Unsteady RANS Simulations of a Shock-Accelerated Heavy Gas Cylinder

B. E. Morgan · **J. A. Greenough**

Received: date / Accepted: date

Abstract Two-dimensional numerical simulations of the Richtmyer -Meshkov unstable "shock-jet" problem are conducted using both large-eddy simulation (LES) and unsteady Reynolds -averaged Navier-Stokes (URANS) approaches in an arbitrary Lagrangian-Eulerian (ALE) hydrodynamics code. Turbulence statistics are extracted from LES by running an ensemble of simulations with multi-mode perturbations to the initial conditions. Detailed grid convergence studies are conducted, and LES results are found to agree well with both experiment and high-order simulations conducted by Shankar, Kawai, and Lele [S. Shankar, S. Kawai, and S. Lele, "Two-dimensional viscous flow simulation of a shock accelerated heavy gas cylinder," Phys. Fluids **23** (2011)]. URANS results using a *k-L* approach are found to be highly sensitive to the initialization of L and to the time at which L becomes resolved on the computational mesh. It is observed that a gradient diffusion closure for turbulent species flux is a poor approximation at early time, and a new closure based on the mass-flux velocity is proposed for low-Reynolds-number mixing.

Keywords Richtmyer-Meshkov instability · turbulent mixing · large-eddy simulation

This work was preformed under the auspices of the U.S. Department of Energy by Lawrence Livermore National Laboratory under Contract No. DE-AC52-07NA27344.

B. E. Morgan
Lawrence Livermore National Laboratory
7000 East Ave., L-170
Livermore, CA 94550 USA
Tel.: +1-925-423-3618
Fax: +1-925-424-2723
E-mail: morgan65@llnl.gov

J. A. Greenough
Lawrence Livermore National Laboratory
E-mail: greenough1@llnl.gov

1 Introduction

Richtmyer-Meshkov instability (RMI) is a fundamental instability in fluids which arises when a shock wave impulsively accelerates the interface between two fluids of different densities [1,2]. In a sense, RMI may be thought of as the impulsive limit of the Rayleigh-Taylor instability (RTI), in which a fluid interface is subjected to constant (usually gravitational) acceleration [3]. Both instabilities arise when perturbations on the interface between two fluids grow due to imposed acceleration. In the case of RMI, a misalignment between the density gradient and the pressure gradient gives rise to the baroclinic generation of vorticity at the interface. By considering the compressible vorticity transport equation, which is given below in Eq. (1) in terms of specific vorticity ($\Omega_i = \omega_i/\rho$), it is easy to identify the baroclinic process as one of three mechanisms for vorticity transport (the other two being *vorticity stretching and tilting* and *viscous transport*) [4]. In this equation, u_i denotes the velocity vector, x_i denotes the coordinate vector, ρ indicates density, p indicates the static pressure, μ is the molecular viscosity, t indicates time, and ε_{ijk} is the permutation tensor. In RMI, baroclinic vorticity generation is the primary mechanism of instability. At later time, secondary instabilities such as the Kelvin-Helmholtz shear instability begin to develop, which lead to the breakup of primary vortical structures and lead ultimately to a region of turbulent mixing [3].

$$\frac{D\Omega_k}{Dt} = \Omega_j \frac{\partial u_k}{\partial x_j} + \underbrace{\frac{1}{\rho^3}\frac{\partial \rho}{\partial x_i}\frac{\partial p}{\partial x_j}\varepsilon_{ijk}}_{\text{baroclinic term}} + \frac{1}{\rho}\varepsilon_{ijk}\frac{\partial^2}{\partial x_i \partial x_j}\left(\mu\left(\frac{\partial u_i}{\partial x_j} + \frac{\partial u_j}{\partial x_i}\right)\right) \tag{1}$$

where

$$\frac{D}{Dt} \equiv \frac{\partial}{\partial t} + u_i \frac{\partial}{\partial x_i} \tag{2}$$

Turbulent mixing processes are important in a wide range of applications, including inertial confinement fusion (ICF) [5], astrophysical phenomena [6], and supersonic combustion [7]. It is therefore important to develop computational tools that are capable of accurately simulating and/or modeling turbulent mixing processes and the fluid instability mechanisms from which these mixing processes arise.

The focus of the present work is on the simulation of a simple RMI configuration, the results of which may be used to inform more complicated simulations of Richtmyer-Meskov-induced mixing in complex geometries and flow regimes. Perhaps the most commonly studied RMI configuration is that of a shocked planar interface. This configuration, which has been studied both experimentally [8,9] and computationally [10], is characterized by an initially linear growth of crests and troughs followed by the nonlinear growth of *spikes* (the penetration of heavy fluid into lighter fluid) and *bubbles* (the rising of light fluid into heavy fluid). Eventually, the spikes roll over, giving rise to the "mushrooming" that is often characteristic of classical RMI [3].

An alternative configuration to the planar interaction just described is the interaction of a planar shock wave with a cylindrical interface. In this configuration, first studied experimentally by Haas and Sturtevant [11] and later by Jacobs [12], the instability enters into a nonlinear regime almost immediately, and the flow is dominated by a pair of counter-rotating vortices which are analogous to the spike features in the planar configuration in the absence of a viscous boundary. The present work focuses on the experimental configuration by Tomkins *et al.* [13] of a planar shockwave interacting with a cylinder of SF_6 in air. The advantage of examining this flow configuration is that during the early time evolution, when the flow is dominated by large counter-rotating vortices, the vorticity field is predominantly two-dimensional. This aspect allows for the careful application of large-eddy simulation (LES) techniques in two dimensions without a significant loss in accuracy. Previous computational studies [14–16] have demonstrated that such a technique may be applied relatively successfully to the simulation of the shock-accelerated heavy gas cylinder.

Although Shankar, Kawai, and Lele [14] have previously demonstrated the ability to accurately reproduce experimental results for the shock-accelerated cylinder problem with a high-fidelity, two-dimensional LES approach, in more complicated applications of turbulent mixing, a high-fidelity approach is often prohibitively expensive. As discussed by Moser and Moin [17] and Kim *et al.* [18], the number of grid points required to resolve the smallest scales of turbulence is expected to scale like $\mathrm{Re}^{9/4}$, and the computational time step should be on the same order as the Kolmogorov timescale. If an LES approach is instead utilized, it is still expected that approximately 80% of the turbulent energy should be resolved on the mesh [19]. An alternative approach is to apply a Reynolds-averaged Navier-Stokes (RANS) approach to model the mixing driven by fluid instabilities such as RMI and RTI. It is the goal of the present work to utilize high-fidelity LES to evaluate the performance of a typical two-equation RANS approach applied to the cylindrical RM problem described above. Specifically, it is intended to leverage the two-dimensional nature of the flow to obtain an ensemble of LES solutions from which turbulence statistics may be extracted and compared against closure terms in the *k-L* RANS model [20].

The remainder of the paper is laid out as follows. First, in section 2, the governing equations are presented along with the generalization of these equations to the LES and RANS approaches used in the present work. Next, in section 3, a description is provided of the arbitrary Lagrangian/Eulerian (ALE) hydrodynamics code that is used in the present study, and the experimental configuration is reduced into a representative numerical model. Then, in section 4, results are presented of simulations of the shocked SF_6 cylinder in air. Finally, in section 5, conclusions are drawn, and recommendations are made concerning the direction of future work.

2 Governing Equations

For the present work, it is assumed that the governing equations for an ideal non-reactive gas mixture are the compressible, multicomponent Navier-Stokes equations, where a Fickian diffusion law is utilized to describe component mass flux. It is also convenient to express conservation of energy in terms of the specific internal energy, e. These governing equations are given explicitly by Eqs. (3) through (6). In these equations, Y_α is used to denote the scalar mass fraction of component α, D_α indicates the binary molecular diffusivity of component α, and δ_{ij} is the Kronecker delta.

$$\frac{D\rho}{Dt} = -\rho \frac{\partial u_i}{\partial x_i} \tag{3}$$

$$\rho \frac{DY_\alpha}{Dt} = \frac{\partial}{\partial x_i}\left(\rho D_\alpha \frac{\partial Y_\alpha}{\partial x_i}\right) \tag{4}$$

$$\rho \frac{Du_j}{Dt} = -\frac{\partial}{\partial x_i}\left(p\delta_{ij} + \sigma_{ij}\right) \tag{5}$$

$$\rho \frac{De}{Dt} = -p\frac{\partial u_i}{\partial x_i} + \frac{\partial}{\partial x_j}\left(u_i\sigma_{ij} - q_j\right) \tag{6}$$

To complete the above equations, the viscous stress tensor, σ_{ij}, and the heat flux vector, q_j, are defined according to Eqs. (7) and (8), respectively. Notice that the heat flux is composed of contributions due to heat conduction and diffusional heat flux [21]. In Eq. (8), κ indicates thermal conductivity, T indicates temperature, and h_α is the specific enthalpy of component α.

$$\sigma_{ij} = \mu\left(\frac{\partial u_i}{\partial x_j} + \frac{\partial u_j}{\partial x_i}\right) - \mu\frac{2}{3}\frac{\partial u_k}{\partial x_k}\delta_{ij} \tag{7}$$

$$q_j = \underbrace{-\kappa\frac{\partial T}{\partial x_j}}_{\text{conduction}} \underbrace{-\sum_{\alpha=1}^{N} h_\alpha \rho D_\alpha \frac{\partial Y_\alpha}{\partial x_j}}_{\text{enthalpy diffusion}} \tag{8}$$

The ideal gas equation of state, $p_\alpha = (\gamma_\alpha - 1)\rho_\alpha e_\alpha$, is used to relate partial pressures to partial densities and partial energies through the ratio of specific heats γ_α, and mixture quantities are computed according to Eqs. (9) [21].

$$p = \sum_{\alpha=1}^{N} v_\alpha p_\alpha, \quad e = \sum_{\alpha=1}^{N} Y_\alpha e_\alpha \tag{9}$$

Component viscosities and mass diffusivities are obtained by application of the Chapman-Enskog method [22]. Mixture viscosity and thermal conductivity are computed using the Wilke rule with Herning and Zipperer approximation [23], and effective binary diffusivities are computed by applying the Ramshaw method [24], which ensures all binary diffusivities sum to zero. Further details on the Chapman-Enskog method and associated mixing rules may be found in Appendix A.

2.1 The *k-L* RANS Model

In general, the RANS equations can be derived from the Navier-Stokes equations by applying a Reynolds decomposition to the primitive variables and by taking an ensemble average of both sides of the governing equations. In the present work, an overbar $\overline{(\cdot)}$ is used to denote an ensemble averaged quantity. Additionally, it is convenient to write the compressible RANS equations in terms of mass-weighted (or Favre) averaged quantities. In the present work, Reynolds decomposition of an arbitrary scalar, f, is denoted by Eq. (10), while Favre decomposition is denoted by Eq. (11).

$$f = \overline{f} + f' \tag{10}$$

$$f = \widetilde{f} + f'' \tag{11}$$

where

$$\widetilde{f} = \frac{\overline{\rho f}}{\overline{\rho}} \tag{12}$$

The RANS model which is investigated in the present work is the *k-L* two-equation model by Dimonte and Tipton [20], which has been developed specifically for its application to the prediction of RTI and RMI growth rates. The *k-L* model has been previously demonstrated to provide good agreement with theoretical growth rates of RTI- and RMI-induced mixing in one dimension [20, 25]. It has been since applied in a wide range of applications including prediction of astrophysical phenomena [26] and simulation of inertial confinement fusion (ICF) targets [27].

Turbulent species flux and turbulent heat flux terms are closed with gradient diffusion arguments. Reynolds stress terms are closed by utilizing the Boussinesq approximation and by solving additional transport equations for a turbulence lengthscale, L, and the turbulence kinetic energy, $k = \frac{1}{2}\widetilde{u_i'' u_i''}$. The *k-L* model is summarized by Eqs. (13) through (22). In these equations, we additionally introduce the notation μ_t to indicate an eddy viscosity, τ_{ij} to indicate the Reynolds stress tensor, and S_{ij} to indicate the strain rate tensor.

$$\frac{D\overline{\rho}}{Dt} = -\overline{\rho}\frac{\partial \widetilde{u}_i}{\partial x_i} \tag{13}$$

$$\overline{\rho}\frac{D\widetilde{Y}_\alpha}{Dt} = \frac{\partial}{\partial x_i}\left[\left(\overline{\rho}D_\alpha + \frac{\mu_t}{N_Y}\right)\frac{\partial \widetilde{Y}_\alpha}{\partial x_i}\right] \tag{14}$$

$$\overline{\rho}\frac{D\widetilde{u}_j}{Dt} = -\frac{\partial \overline{p}}{\partial x_j} + \frac{\partial}{\partial x_i}\left(\overline{\sigma}_{ij} + \overline{\rho}\tau_{ij}\right) \tag{15}$$

$$\begin{aligned}\overline{\rho}\frac{D\widetilde{e}}{Dt} =& -\overline{p}\frac{\partial \widetilde{u}_i}{\partial x_i} + b_t\frac{\mu_t}{\overline{\rho}^2}\left(\frac{\partial \overline{\rho}}{\partial x_i}\frac{\partial \overline{p}}{\partial x_i}\right) + d_t\frac{\overline{\rho}k^{3/2}}{L} \\ &+ \frac{\partial}{\partial x_j}\left[\widetilde{u}_i\overline{\sigma}_{ij} - \overline{q}_j + \frac{\mu_t}{N_e}\frac{\partial \widetilde{e}}{\partial x_j}\right]\end{aligned} \tag{16}$$

$$\begin{aligned}\overline{\rho}\frac{Dk}{Dt} =& -b_t\frac{\mu_t}{\overline{\rho}^2}\left(\frac{\partial \overline{\rho}}{\partial x_i}\frac{\partial \overline{p}}{\partial x_i}\right) + \overline{\rho}\tau_{ij}\frac{\partial \widetilde{u}_i}{\partial x_j} \\ &- d_t\frac{\overline{\rho}k^{3/2}}{L} + \frac{\partial}{\partial x_i}\left[\left(\mu + \frac{\mu_t}{N_k}\right)\frac{\partial k}{\partial x_i}\right]\end{aligned} \tag{17}$$

$$\overline{\rho}\frac{DL}{Dt} = C_c\overline{\rho}L\frac{\partial \widetilde{u}_i}{\partial x_i} + C_L\overline{\rho}\sqrt{2k} + \frac{\partial}{\partial x_i}\left(\frac{\mu_t}{N_L}\frac{\partial L}{\partial x_i}\right) \tag{18}$$

where

$$\mu_t = a_t \overline{\rho} L k^{1/2} \tag{19}$$

$$\overline{\rho}\tau_{ij} = 2\mu_t \overline{S}_{ij} - \frac{2}{3}\overline{\rho} k \delta_{ij} \tag{20}$$

$$\overline{S}_{ij} = \frac{1}{2}\left(\frac{\partial \tilde{u}_i}{\partial x_j} + \frac{\partial \tilde{u}_j}{\partial x_i}\right) - \frac{1}{3}\frac{\partial \tilde{u}_k}{\partial x_k}\delta_{ij} \tag{21}$$

$$\overline{\sigma}_{ij} = 2\mu \overline{S}_{ij} \tag{22}$$

In the present work, two sets of model constants are investigated, both of which are consistent with one-dimensional self-similarity analysis. Simulations are performed using the standard Dimonte and Tipton coefficient set [20], which was derived assuming a Rayleigh-Taylor bubble growth rate of $\alpha_b = 0.060$; additionally, we explore results using a new coefficient set, which is derived in Appendix B and assumes a lower growth rate of $\alpha_b = 0.025$. The two coefficient sets are summarized in table 1.

3 Numerical Models

For the present study, the *Ares* arbitrary Lagrangian/Eulerian (ALE) hydrodynamics code developed at Lawrence Livermore National Laboratory (LLNL) is utilized. The block-structured *Ares* code solves the governing equations described in the previous section in a Lagrangian coordinate frame, and a second-order remap scheme [28] is then applied to avoid mesh tangling and associated computational difficulties. In order to compare most directly with previous computational work [14], the present work utilizes a fixed Eulerian mesh.

Explicit time integration is accomplished with a second-order predictor-corrector scheme [29], and spatial differences are computed with a non-dissipative second-order finite element approach. A tensor artificial viscosity [30] is applied for the capturing of shocks and material discontinuities.

The *Ares* code additionally utilizes adaptive mesh refinement (AMR) [31,32] to localize computational grid points in regions of interest. In the present work, this capability is utilized to improve computational efficiency by clustering gridpoints around the shock interface and the heavy gas cylinder. More details on the computational domain are provided in section 3.4.

3.1 LES in Two Dimensions

It is well-established that two-dimensional turbulence is fundamentally different from three-dimensional turbulence [19, 33]. This difference follows from the fact that the vortex stretching term in the vorticity equation vanishes in two dimensions, and the remaining vorticity term evolves, essentially, as a conserved scalar. As a result, energy in two-dimensional turbulence is generally transferred up the cascade from the small scales to the large, rather than from the large scales to the small as in canonical three-dimensional turbulence [34]. Although most physical flows are naturally subject to three-dimensional instabilities [35], in the special circumstance of a flow heavily confined by geometry or by applied body forces, a flow may be two-dimensional or quasi-two-dimensional in nature [33].

A number of previous computational studies [14–16] have all demonstrated that the shocked gas cylinder problem presently under consideration can be simulated accurately with a two-dimensional approximation. Additionally, Weirs *et al.* [36] have compared two-dimensional and three-dimensional calculations of the experiment by Tomkins *et al.* [13] and shown that three-dimensional effects are generally negligible until relatively late time (after about 750 μs). We therefore exploit the quasi-two-dimensional nature of the flow at early time in order to justify the careful application of LES in two-dimensions. The advantage of this approach is that it allows for the efficient collection of turbulence statistics by running an ensemble of simulations; although those statistics no doubt contain error due to the reduction in dimensionality, it is expected that such errors should be relatively small during early time evolution.

3.2 Sub-grid Scale (SGS) Model

In the present work, an implicit LES approach is utilized [37, 38]; that is, no explicit model is used to solve for the subgrid turbulent contributions to the filtered governing equations. Of course, this approach relies on the inherent dissipation of the numerical scheme to provide stability and subgrid energy transfer [39,40]. Much work has been done to establish the validity of the implicit LES approach for the simulation of both three-dimensional [41,42] and two-dimensional flows [34]. It is important to note, however, that the present work computes the resolved molecular transport (viscosity, diffusivity, and thermal conductivity) according to the Chapman-Enskog method as discussed in Appendix A and relies on numerical dissipation for only the *subgrid* contribution; this approach is in contrast to much of the literature on implicit LES, which often solves the filtered Euler equations and relies on an assumption of flow in the limit of high Reynolds number to justify numerics (and by exten-

Table 1 *k-L* Model Constants

	α_b	a_t	b_t	d_t	C_C	C_L	N_Y	N_e	N_k	N_L
Standard Set	0.060	1.414	1.20	3.50	1.00	1.00	1.00	1.00	1.00	0.50
New Set	0.025	0.290	3.50	1.00	0.33	0.28	0.14	0.14	0.14	0.07

sion, the subgrid scale) as the dominant contributor to dissipation.

By including the effects of molecular transport in the present simulations, it is possible to more accurately quantify the effects of the numerical relative to the physical dissipation and thereby assess solution quality. The present work, therefore, emphasizes the use of detailed grid resolution study to obtain nearly grid-converged LES results.

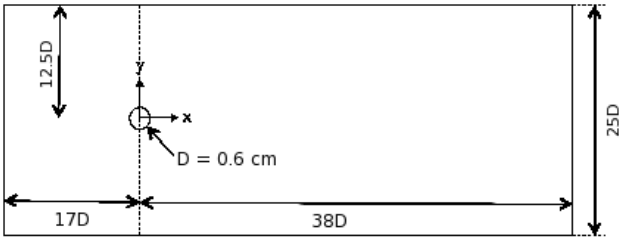

Fig. 1 Computational domain (not to scale)

3.3 Initial Conditions

Initial conditions are chosen to match those of the experiment by Tomkins *et al.* [13] and simulations by Shankar, Kawai, and Lele [14]. Specifically, a cylinder (circular region, in two dimensions) of SF_6 gas is located in initially quiescent air (which is assumed to be a 79:21 mixture of N_2 and O_2 gas) and impacted by a Mach 1.21 shock wave. Initial pressure and temperature in the stationary unshocked gas are 0.8atm and 298K, respectively. Initial velocity and thermodynamic conditions in the shocked gas are given by the Rankine-Hugoniot jump conditions. The initial concentration of SF_6 gas is given by Eq. (23) in terms of the cylinder radius, R_d, and the maximum concentration, Y^0_{max}, which was determined experimentally [13,36] to be 0.83.

$$Y^0_{SF_6}(r,\theta) = \begin{cases} Y^0_{max}\left(1.0-\exp\left(\frac{-\left|\left(\frac{|r-\eta|}{R_d}-1\right)\pi\right|^{1.54}}{1.0082}\right)\right) & |r|\le R_d \\ 0.0 & |r|>R_d \end{cases} \quad (23)$$

In the above profile, $\eta(r,\theta)$ represents a multimode perturbation function. For baseline simulations, we take $\eta = 0$. Later, to obtain turbulence statistics from LES, an ensemble of simulations are run, where the perturbation function is given by Eq. (24). In this equation, the maximum amplitude $A = 0.035R_d$ is chosen to match experimental error bars reported by Tomkins *et al.* [13], and ϕ indicates a random phase shift in $[-\pi,\pi]$.

$$\eta(r,\theta) = \sum_{k=0}^{14} 2\frac{A}{15}\sin(k\theta+\phi)\cos(k\theta+\phi) \quad (24)$$

To initialize turbulence quantities in the *k-L* RANS model, initial turbulence kinetic energy is set to a near-zero positive value everywhere ($k(x,y)$ = 1e-32). Additionally, two initialization strategies are utilized to set the initial turbulence lengthscale, L_0, in the gas cylinder. In the first case, L_0 is held constant in the cylinder at 0.01 μm (well below the grid lengthscale), and in the second case, L_0 is specified in terms of the finest mesh spacing, Δ, such that L_0/Δ is held constant at 0.5, enforcing a mesh dependence on the initial lengthscale. This second choice is motivated by work by Johnson and Schilling [43,44], who have shown that for simulations with a discontinuous mean flow, the growth rates obtained using two-equation RANS models tend to scale with grid resolution. It is also worth noting that Dimonte and Tipton [20] similarly observed a sensitivity of the realized growth rate to initial conditions, although they did not tie this sensitivity to the mesh resolution. Indeed, Johnson and Schilling argue that the lack of convergence they observed when holding a constant initial lengthscale was due to unresolved interfaces in the initial conditions, "analogous to the lack of convergence in a shock width in a shock-capturing simulation [43]." It is therefore anticipated that this second initialization strategy might provide better convergence behavior than the first.

3.4 Computational Domain and Boundary Conditions

The mesh used in the present study is Cartesian and planar, parameterized by the diameter of the SF_6 cylinder ($D = 2R_d$ = 0.6 cm). The center of the cylinder is located at the origin, and the mesh extends from -17D to 38D in the streamwise (x) dimension and from -12.5D to 12.5D in the stream-normal dimension (y), as illustrated by Fig. 1. A depth of 1 cm is assumed in spanwise (z) dimension when computing volume-integrated quantities.

The problem is solved in a laboratory fixed coordinate frame such that the shock, initially located at x = -1.5D, is

Table 2 Computational mesh parameters

Mesh	N_x^1	AMR Levels	cells/D	Δ (μm)
A	100	4	82	72.3
B	100	5	245	24.5
C	100	6	736	8.15
D	200	6	1473	4.07
E	100	7	2209	2.72
F	200	7	4418	1.36

observed to propagate from left to right at a speed of Mach 1.21.

As discussed earlier, the *Ares* code utilizes AMR to localize computational cells in regions of interest. In the present problem, AMR is utilized to cluster cells along the shock interface and in regions of non-zero SF_6 mass fraction such that the cylinder is entirely resolved on the finest level of mesh refinement. For each level of grid refinement beyond the first, the mesh is refined by adding an additional factor of 3 cells in each dimension. At the first level of grid refinement, the mesh is refined by a factor of 5 cells in each dimension. Cells are nominally square; therefore, the computational domain is completely parameterized by the number of cells in the x-dimension on the coarsest level (N_x^1) and by the number of levels of AMR refinement. Table 2 summarizes those meshes which are used in the present study.

Boundary conditions at the inflow fix velocity and thermodynamic conditions of the shocked gas. Outflow boundary conditions fix gas velocity and are time dependent such that they "swallow" the primary shock. This ensures the primary shock is not reflected, and therefore re-shock of the SF_6 cylinder is not simulated. Upper and lower boundaries are non-reflecting "sponge" boundaries that are also time dependent (to account for the location of the primary shock) and allow perturbations in velocity and thermodynamic variables to go smoothly to zero. These sponge boundary conditions ensure that spurious acoustic reflections do not interfere with the region of interest around the SF_6 gas cylinder.

4 Results and Discussion

Having presented the theoretical and computational framework for the present investigation, it is now possible to proceed with analysis of results obtained with LES and RANS simulations of the shock-jet flow. To begin, it is useful to first establish confidence in a baseline solution to which all other simulations may be compared. To this end, baseline validation efforts in this section will focus on comparisons with high-order LES results by Shankar, Kawai, and Lele [14]. These comparison results, which were obtained with a sixth-order compact differencing scheme utilizing localized artificial diffusivity for SGS modeling and shock capturing [45], have been shown to be nearly grid converged with 960 grid points across the cylinder. Additionally, the comparison LES results were simulated with zero initial perturbation to the SF_6 cylinder with acetone excluded. Indeed it has been shown [14] that the unquantified amount of acetone present in the experimental gas cylinder (which was used for imaging purposes) is expected to significantly affect results. The simulations by Shankar, Kawai, and Lele [14] are therefore expected to be more directly comparable to the present results than the experiment by Tomkins *et al* [13].

4.1 Baseline LES results

Figure 2 plots mass fraction contours of SF_6 obtained by LES with no initial perturbation for several levels of grid resolution. This figure illustrates that good qualitative agreement is obtained for mesh resolutions C and above. Specifically, it can be seen that the secondary Kelvin-Helmholtz instabilities that begin to appear between 400 and 490 μs are not well captured on meshes A and B. It is also observed that the comparison results generally predict less secondary instability in the primary vortices beyond about 400 μs than the present work. This may be a result of the artificial viscosity which is present in the comparison results.

To quantify the effect of grid resolution on the solution, Fig. 3 plots two measures of mixing in the problem for mesh resolutions A through F. First, the total mix mass, given by Eq. (25), provides a measure of the total quantity of mixed fluid in the problem. Additionally, the total mixing rate (TMR), given in general by Eq. (26), provides an integral description of the instantaneous scalar dissipation rate [13].

$$\text{total mix mass} = \int \rho Y_{SF_6} \left(1 - Y_{SF_6}\right) dV \tag{25}$$

$$\text{TMR} = \frac{1}{\left(Y^0_{max}\right)^2} \int D_{SF_6} \left(\frac{\partial Y_{SF_6}}{\partial x_i}\right)^2 dV \tag{26}$$

Both the total mix mass and the total mixing rate demonstrate a clear trend towards grid convergence, with little difference observed in either quantity beyond mesh resolution level E. The total mixing rate shows more sensitivity to grid resolution; fortunately, comparison data for this quantity is available from both experiment [13] and high-fidelity simulation [14]. Although comparison with these data sets shows that the present simulations appear to converge to a higher initial mixing rate, good agreement is obtained in both the time and magnitude of peak mixing rate as well as in prediction of late time mixing. The observed discrepancy in early time mixing rate, however, is likely related to the previously discussed secondary instabilities in the primary vortical structures. Specifically, the present work predicts earlier

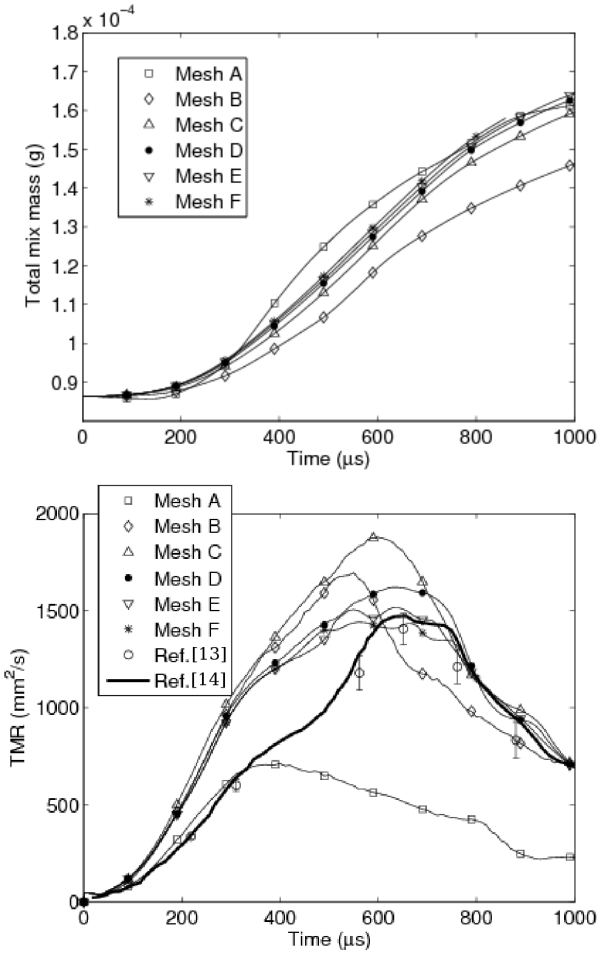

Fig. 3 Two measures of mixing using LES with no initial perturbation: total mix mass (top) and total mixing rate (bottom)

onset of secondary instabilities in the primary vortex cores, which likely leads to the higher rate of mixing. Although the results by Shankar, Kawai, and Lele [14] demonstrate better agreement with experiment during the early time mixing, it is not clear that the simulations should agree so well with experiment, which is additionally complicated by the presence of an unknown amount of acetone (an effect which is neglected in both sets of simulations).

Figure 4 further explores the effect of grid resolution on more sensitive indicators of vortex intensity by plotting total enstrophy as a function of time for mesh resolutions A through F. Enstrophy, defined by Eq. (27) in terms of the spanwise component of vorticity ω_z and normalized by the total area A, provides an integral measure of total vorticity. A high degree of grid convergence is observed in enstrophy for resolution meshes D and higher, which indicates that the effect of numerical dissipation is low for these resolution levels.

$$\text{enstrophy} = \frac{1}{A}\iint \omega_z^2 dxdy \tag{27}$$

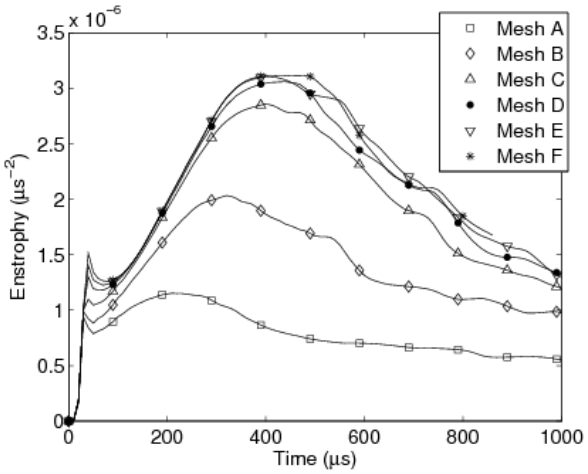

Fig. 4 Enstrophy as a function of grid resolution using LES with no initial perturbations

By comparison, Fig. 5 plots two quantities of interest obtained from inviscid simulation against results from highly resolved (Mesh E) viscous simulation. First, by plotting total mix mass, it is seen that although the inviscid simulations may demonstrate a trend towards convergence, the total mixing in the resolved simulations is less than in the viscous simulations. Since the effect of viscosity is generally to suppress fine scale mixing, the observed increase in the viscous mix mass may therefore be attributed to molecular diffusion of species. Interestingly, the very coarse (Mesh A) inviscid simulation is observed to agree quite well in total mix mass with the viscous simulation due to the high level of numerical dissipation in this simulation. Indeed, both the viscous and inviscid simulations at A-level resolution are quite comparable in measures such as total mix mass, which indicates that at the low resolution, numerical dissipation dominates molecular diffusion. Of course, when total mix mass is captured at low resolution, total vorticity is severely under-predicted. Moreover, as demonstrated by the bottom plot in Fig. 5, without the physical regularization effect of molecular viscosity, the inviscid simulations will necessarily fail to converge in high-order measures of vorticity such as enstrophy.

Mesh resolution studies on enstrophy such as those in Figs. 4 and 5 additionally provide some insight into the range of turbulence lengthscales which are resolved in the present viscous simulations. Ideally, large-eddy simulations should resolve well into the inertial subrange of the turbulence spectrum. In two-dimensional simulations such as those in the present study, which do not have a homogeneous dimension over which to compute instantaneous ensemble average quantities, it is difficult to compute turbulence spectra directly. However, the convergence in enstrophy observed in viscous simulations, combined with the over-shoot in enstrophy observed in inviscid simulations, suggests that vis-

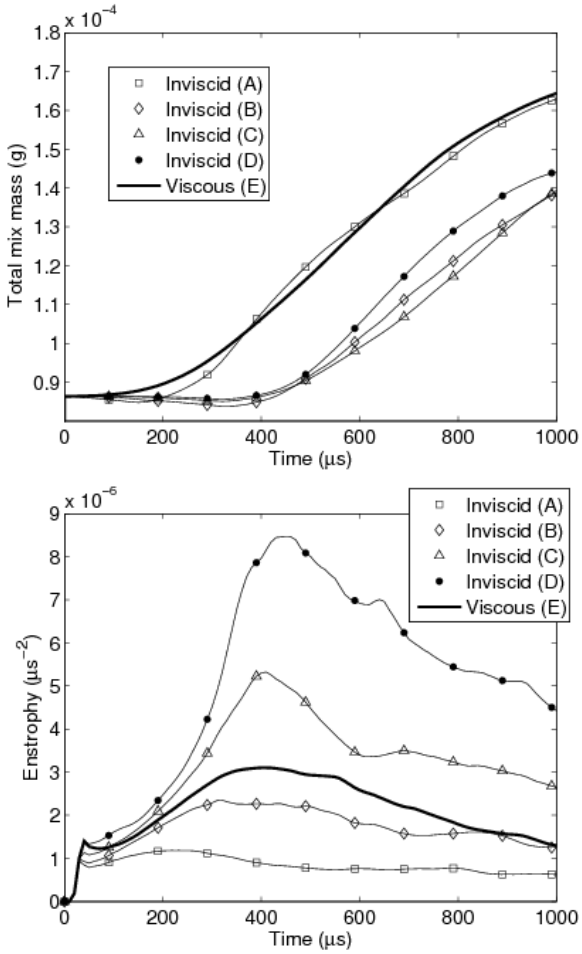

Fig. 5 The effect of molecular transport through comparison with inviscid simulation: total mix mass (top) and enstrophy (bottom)

cous simulations with resolution level D and above are resolving sufficiently near the dissipation range of turbulence.

4.2 Ensemble LES Results

In order to directly assess the quality of RANS simulations of the shock-jet problem, it is necessary to consider turbulence statistics and mean profiles which cannot be obtained from a single two-dimensional simulation. Ideally, turbulence statistics would be obtained from high-fidelity three dimensional simulation. Given the computational expense of the problem under consideration, however, such an approach is not feasible. As a compromise, a large number of high-resolution two-dimensional simulations can be run, with perturbed initial conditions (as discussed previously in section 3.3). Of course, this approach will not provide accurate statistics when fluctuations into the plane of simulation would become significant relative to fluctuations in x and y. Fortunately, for the problem under consideration, it is expected that this should be a reasonable approximation at least until late time transition to turbulence (beyond about 560 μs).

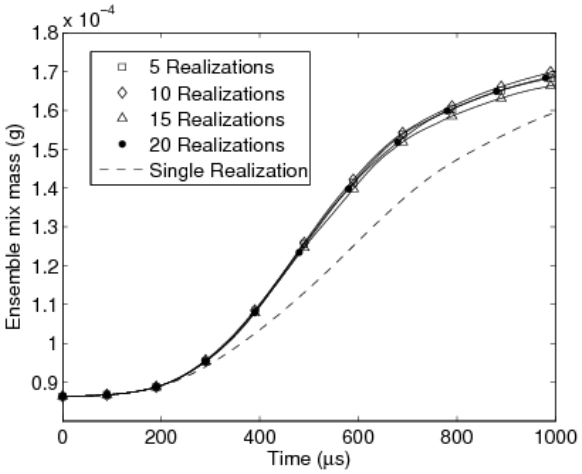

Fig. 7 Convergence of ensemble mix mass as a function of ensemble size.

To obtain statistics as a baseline for comparison with RANS, 20 LES realizations of the shock-jet problem are run at level-C mesh resolution with initial conditions perturbed according to Eq. (24). When computing ensemble averages, in order to reduce statistical noise, averages are taken over the 20 realizations and then about the plane at $y = 0$. Figure 6 illustrates qualitatively how perturbations in initial conditions can lead to significant differences at late time and how a baseline ensemble may be obtained by averaging over multiple realizations.

Figure 7 plots the ensemble mix mass, given by Eq. (28), for ensembles of 5, 10, 15, and 20 realizations; this plot indicates good statistical convergence for ensemble mix mass and suggests that similar integral measures may be reasonably considered converged over the 20 realizations considered. It is also interesting to note in Fig. 7 the difference between the ensemble mix mass and the total mix mass calculated from the single baseline simulation. It can be shown [46] that the ensemble mix mass is expected to be greater than the instantaneous mix mass by a factor approximately equal to the integrated scalar variance, $\overline{Y'_{SF_6} Y'_{SF_6}}$.

$$\text{ensemble mix mass} = \int \overline{\rho} \widetilde{Y}_{SF_6} \left(1 - \widetilde{Y}_{SF_6}\right) dV \tag{28}$$

Figure 8 furthermore demonstrates the effect of initial conditions on late-time mixing in the LES database by plotting total mix mass and total mixing rate along with error bars indicating two standard deviations over all 20 realizations. Note that this figure shows the mean total mix mass obtained by averaging the temporal mix mass histories of all 20 realizations. This is a different quantity than the ensemble mix mass, as defined in Eq. (28). From this image, it

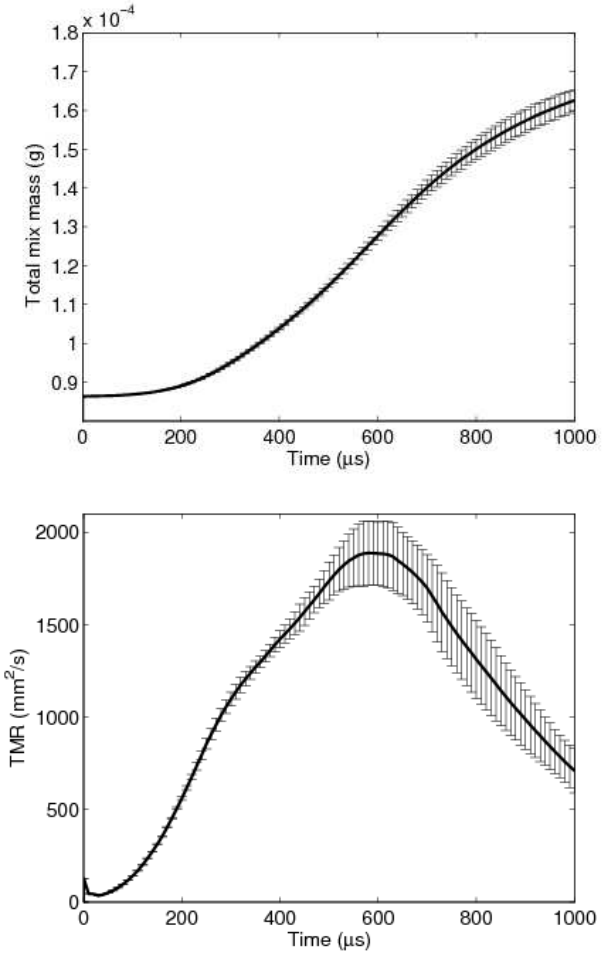

Fig. 8 Effect of initial conditions on total mix mass (top) and total mixing rate (bottom). Solid black lines represent mean over 20 realizations, and errorbars indicate two standard deviations.

is clear that the effect of initial conditions does not significantly affect reproducibility until around 500 μs. This image should also provide some sense of the approximate transition to turbulence, as variance in TMR should correspond to an increase in magnitude of turbulent mixing correlations.

In addition to mean quantities, having an ensemble database of LES simulations allows for the extraction of turbulence statistics. Figure 9 illustrates the 2D Reynolds stress components extracted from the LES database. In this figure, the diagonal terms are plotted on the same color scale, and the shear stress component is plotted on a scale with magnitude half that of the other two components. It is interesting to note that regions of τ_{11}/τ_{22} anisotropy seem to be mostly localized. For instance, the τ_{22} component seems to dominate at the center of vortex cores, and the τ_{11} component seems to dominate along the interior of the first roll-up where the left/right vortex interaction is strongest. Otherwise, in general there does not appear to be significant τ_{11}/τ_{22} anisotropy. Of course, it is impossible to comment on anisotropies with respect to τ_{33} using 2D simulations.

Similarly, Figs. 10 and 11 plot the contributions to turbulent species diffusion that are closed in Eq. (14) with a gradient diffusion approximation. By plotting the turbulence terms next to the mean gradient components, however, it is clear that the two terms demonstrate significantly different patterns of symmetry and antisymmetry. For instance, the mean streamwise gradient demonstrates a change in sign from the top to the bottom of the cylinder, which does not appear in the streamwise turbulent transport term. (Due to rotation of the cylinder in the image, this change is actually along a plane of constant y coordinate.) Qualitatively, such observations suggest that gradient diffusion may not be a good assumption to close these terms during the early phase evolution.

4.3 *k-L* Results With Standard Coefficient Set

Having established a high-fidelity LES database to which we can compare, attention is now shifted to results obtained using the *k-L* RANS model. One additional complication which is introduced by the RANS model is the necessity for initial conditions on the additional transported turbulence quantities k and L. Since k is representative of turbulence kinetic energy (TKE) and the flow is assumed initially free of turbulence, k may be reasonably assumed to be zero throughout the flow. Unfortunately, the *k-L* model formulation requires a non-zero value for the initial lengthscale, L_0. This initial value is often interpreted as the lengthscale of initial perturbations (which often is not well characterized in experiment) [20]; although a more precise interpretation might be that L_0 is the lengthscale associated with energy-bearing eddies, often measured as the integral lengthscale, related to k and TKE dissipation, ε, through Taylor's relation $L \backsim \frac{k^{3/2}}{\varepsilon}$ in fully developed turbulence [47].

Since there is significant uncertainty associated with both the interpretation and the knowledge of initial lengthscales in the flow, two different approaches are investigated in the present work for the initialization of L. In the first approach, the initial lengthscale is chosen to be equal to a constant value much less than the finest resolved scale on all meshes, $L_0 = 0.01\mu m$. This approach is consistent with the interpretation of L_0 as a known, consistent perturbation lengthscale. In the second approach, the initial lengthscale is chosen to be equal to one half of the finest mesh spacing, $L_0 = \Delta/2$. This approach enforces a mesh-dependence on the initial conditions for L and is less consistent with a physical interpretation of the lengthscale L.

Figures 12 and 13 illustrate qualitatively the results obtained with the *k-L* model using the two different initialization strategies. Firstly, it seems that the RANS results generally start by resolving the primary vortical structures for some amount of early time before quickly becoming

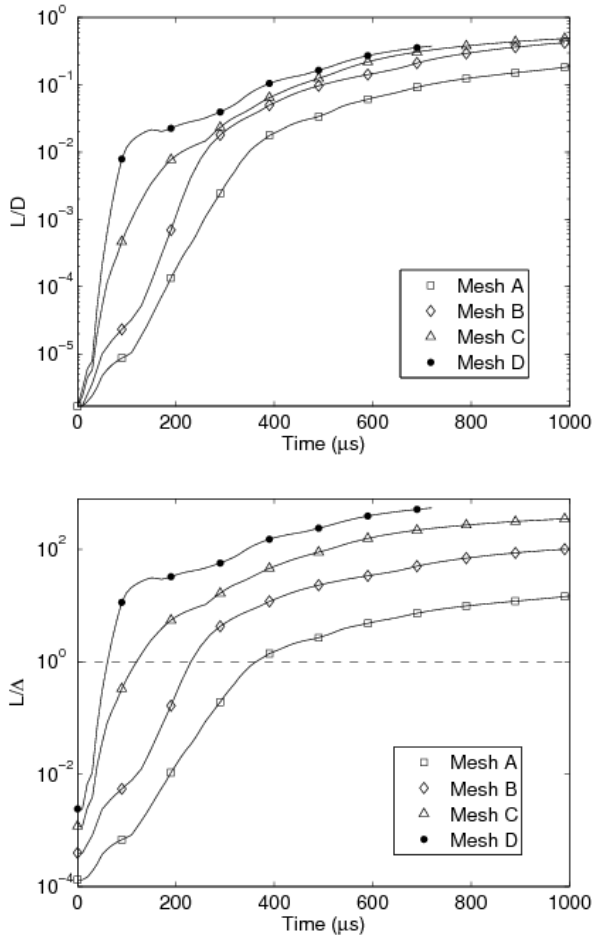

Fig. 14 Growth of maximum L using *k-L* RANS model with constant $L_0 = 0.01\mu m$. Lengthscale normalized by cylinder diameter (top) and by mesh spacing (bottom).

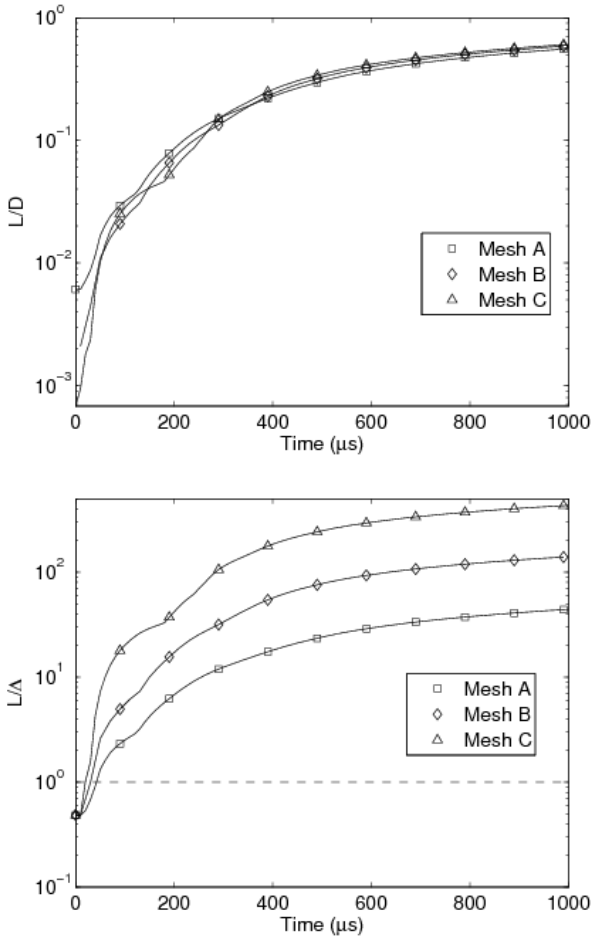

Fig. 15 Growth of maximum L using *k-L* RANS model with mesh-dependent $L_0 = \Delta/2$. Lengthscale normalized by cylinder diameter (top) and by mesh spacing (bottom).

"blurred". Interestingly, and perhaps counter-intuitively, it appears that those results with mesh-dependent initial conditions for L_0 (illustrated in Fig. 13) seem to demonstrate better grid convergence properties than those results obtained with a constant L_0. As discussed previously in section 3.3, this sensitivity is most likely attributable to a lack of convergence in unresolved initial interfaces [43]. Indeed, for the levels of resolution considered, it is clear that those results obtained with a constant L_0 do not demonstrate grid convergence. Specifically, for those results obtained with a constant L_0, increasing the grid resolution appears to induce an earlier onset of "blurring" in the solution, which suggests that the growth rate of L (and therefore mixing in the solution) must be highly sensitive to the time at which L becomes resolved on the mesh (that is, the time at which $L/\Delta = 1$), which we shall denote by t_{res}. This observation is confirmed quantitatively in Figs. 14 and 15, which plot maximum L as a function of time and mesh resolution for both initialization approaches. In Fig. 14, which plots the growth of L for a constant L_0, it is clear that the growth of L is very much dependent on the mesh resolution, and there is no clear trend towards convergence at early time. For constant initial conditions, $t_{res} \approx 65\ \mu s$ on mesh D, 120 μs on mesh C, 230 μs on mesh B, and 365 μs on mesh A. It appears that qualitative onset of "blurring" always occurs after t_{res} in the previously discussed plots of SF_6 mass fraction, which suggests that the value of L may be acting something like a filter width for ensemble averaging. By contrast, Fig. 15, which plots the growth of L for constant L_0/Δ demonstrates surprising convergence in L/D for both early and late time. In these simulations, $t_{res} \approx 45\ \mu s$ on mesh A, 30 μs on mesh B, and 20 μs on mesh C. As a result of this lesser variation in t_{res}, the time evolution of L/D demonstrates much better grid convergence properties, a fact which is undoubtedly related to the qualitative similarities in SF_6 mass fraction previously commented upon in regards to Fig. 13.

The implications of the observed grid sensitivities to integral mixing are considered in Fig. 16 which plots total mix mass for the two initialization strategies. It is clear that the results with mesh-dependent L_0 demonstrate less sensitiv-

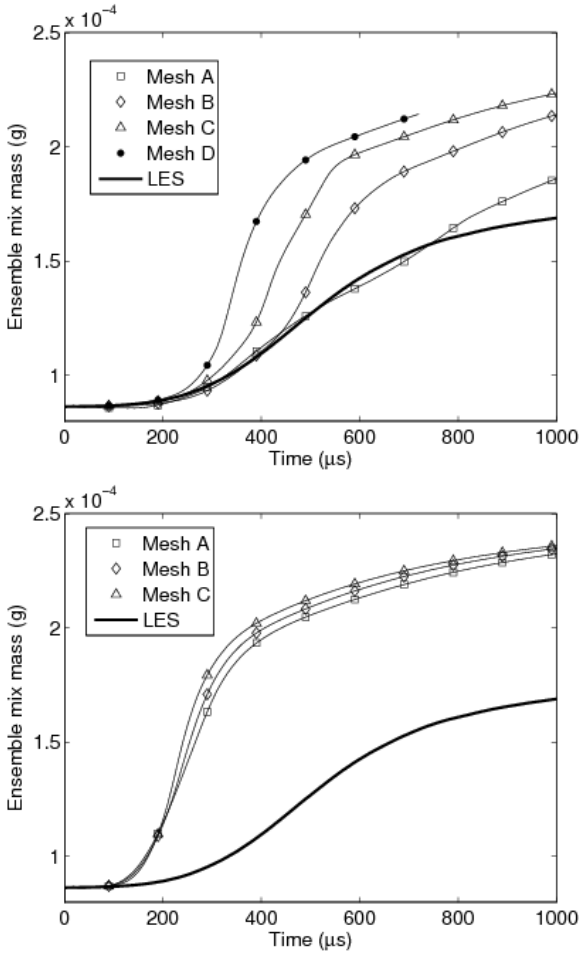

Fig. 16 Ensemble mix mass as a function of grid resolution for constant $L_0 = 0.01\mu m$ (top) and mesh-dependent $L_0 = \Delta/2$ (bottom) using standard *k-L* coefficient set.

ity to mesh resolution than those with constant L_0. Perhaps most troubling is the fact that, with constant L_0, increasing mesh resolution both increases ensemble mix mass and moves the solution further away from the ensemble LES result – implying that solution quality gets worse with increasing mesh resolution. Of course, the results with mesh-dependent L_0 seem to imply that once L is resolved on the mesh, the evolution of L is relatively insensitive to grid resolution. Therefore, it might be anticipated in the first case that if grid resolution were continually increased to the point where $\Delta \approx 0.01\mu m$, a converged solution might be anticipated. However, trends in the mix mass curve suggest that such a converged solution might look very much like the results obtained for $L_0/\Delta = 0.5$.

Figure 17 further investigates the issue of mesh sensitivity by plotting several turbulence parameters from the case of initially unresolved $L_0 = 0.01\mu m$ on mesh C. Notice in this figure that contours of the ratio L/Δ are plotted from 0 to 100. By plotting the turbulence lengthscale in this way, contours only become visible when L is greater than the grid scale. Between 220 μs and 310μs, the first contours of L become visible, and k begins to grow rapidly in these regions. Beyond 310 μs, it is striking to see that the region over which $L/\Delta > 1$ roughly corresponds to a qualitative region of "blurring" in the mass fraction field, indicating that this is where turbulent diffusion is most active. Unfortunately, the rate at which this process occurs seems to be much greater than what is observed in the LES ensemble.

4.4 *k-L* Results With New Coefficient Set

One possibility that might explain the over-prediction of mixing observed with the standard *k-L* prescription is that the model is calibrated to predict a growth rate that is simply too high. As discussed previously, the standard coefficient set for the *k-L* model is derived assuming a Rayleigh-Taylor bubble growth rate $\alpha_b = 0.060$. This value seems to agree well with the majority of experimental evidence but seems to be significantly higher than the majority of previous computational studies [48]. One theory that has been proposed to explain this discrepancy is that mixing immiscible fluids might be expected to have a higher RT growth rate than their miscible counterparts. In such a case, simulations of miscible gases might be expected to predict a lower α_b than experiments which have generally been conducted with immiscible liquids. As described in Appendix B, a new *k-L* coefficient set can be derived assuming a lower $\alpha_b = 0.025$, which is more in line with previous computational studies [48].

Figures 18 and 19 summarize results obtained with the new *k-L* coefficient set ($\alpha_b = 0.025$) for constant $L_0 = 0.01\mu m$ and mesh-dependent $L_0 = \Delta/2$ initial conditions, respectively. By comparing these figures with Figs. 14 and 15, it is clear that the new coefficient set leads, as expected, to less mixing. Indeed, reasonable qualitative agreement seems to be obtained between the LES ensemble SF_6 contours and the results obtained with the new set at C-level mesh resolution for the $L_0 = 0.01\mu m$. Unfortunately, the sensitivity to mesh resolution seems to remain, although it is not quite as extreme as observed previously in Fig. 18. Although having resolved initial conditions again seems to improve convergence properties, as illustrated in Fig. 19, this initialization approach continues to lead to results with far too much mixing.

Figure 20 quantifies the observations that were drawn from Figs. 18 and 19 by plotting ensemble mix mass for the two initialization strategies. Compared to results with the standard coefficient set (Fig. 16), results with the new coefficient set demonstrate less overall mix mass. Simulations with a constant, unresolved initial L_0 indeed seem to bracket the LES ensemble result; however, it is clear that increasing mesh resolution in this case leads to increasing mix mass. Figure 21 additionally plots the time evolution

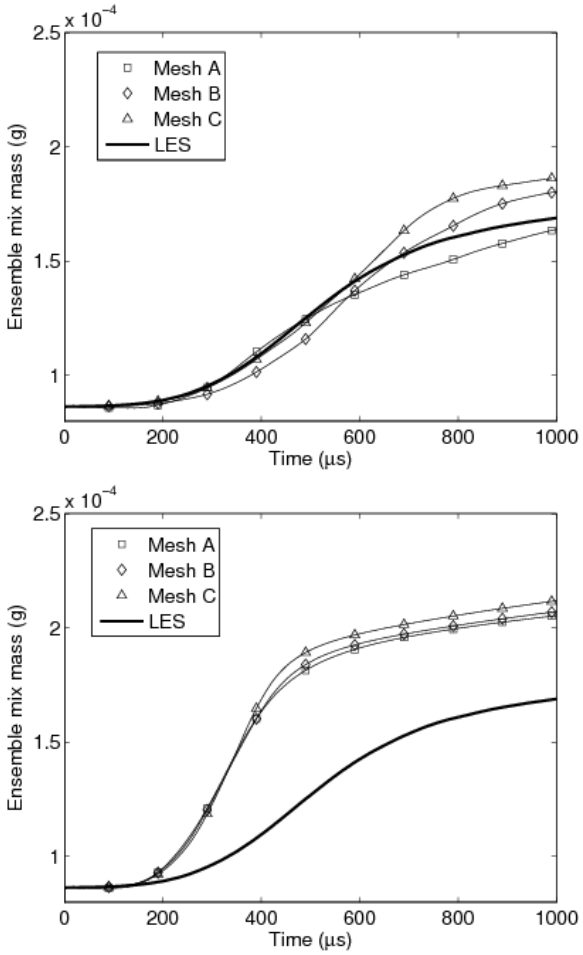

Fig. 20 Ensemble mix mass as a function of grid resolution for constant $L_0 = 0.01\mu m$ (top) and mesh-dependent $L_0 = \Delta/2$ (bottom) using new *k*-*L* coefficient set.

of turbulence parameters for $L_0 = 0.01\mu m$ on mesh C. In this figure, we see that although the magnitude of L tends to be less than that predicted by the standard coefficient set, the magnitude of k is much greater. It is particularly interesting to note the extreme change in magnitude of k that occurs between 220 μs and 310μs, around the time when L first becomes resolved on the mesh. Figure 22 compares the magnitude of k predicted by the two RANS approaches with TKE extracted from the LES ensemble simulations. Although RANS results with the standard coefficient set appear to agree better with LES in terms of overall magnitude of TKE, it is clear that neither RANS simulation agrees with LES in the growth rate or spatial distribution of TKE. Specifically, where the LES results show peaks of TKE localized in the vortex cores, the RANS simulations predict a more homogenized TKE field, distributing TKE relatively uniformly throughout the mixing region.

4.5 A Potential Improvement for RANS Simulation of Low-Reynolds Number Mixing

As we have seen in the previous two subsections, simulation of the shock-jet problem with the *k*-*L* RANS model, regardless of the coefficient set used, tends to predict too much mixing. At issue seems to be the fact that assumptions of homogeneity of turbulence, which are built into the model closures, may not be appropriate for early-time evolution when the Reynolds number is low and the flow has not fully transitioned to turbulence. As illustrated previously in the context of Figs. 10 and 11, the gradient diffusion approximation seems particularly ill-suited for closing the turbulent species flux during this time. Specifically, models relying on gradient diffusion to close turbulent species flux make the following approximation.

$$\overline{\rho u_i'' Y_\alpha''} \approx -\frac{\mu_t}{N_Y}\frac{\partial \widetilde{Y}_\alpha}{\partial x_i} \tag{29}$$

In addition to k and L, however, some models such as the BHR family [49] additionally solve transport equations for the mass-flux velocities, $\overline{u_i''}$. Figure 23 plots these terms, as extracted from the LES database. It is interesting to note that these terms exhibit very similar qualitative behavior compared to the turbulent mass flux terms $\overline{\rho u_i'' Y_{SF_6}''}$, plotted previously in Figs. 10 and 11. To examine this idea in more detail, let us denote the angle between the turbulent species flux vector and the mean scalar gradient vector by $\theta_{\nabla\widetilde{Y}_{SF_6}}$. Similarly, let us denote the angle between the turbulent species flux vector and the mass-flux velocity vector by $\theta_{\overline{u_i''}}$. It is expected that in regions where the angle $\theta_{\nabla\widetilde{Y}_{SF_6}}$ is large, the gradient diffusion closure should be inaccurate. Fig. 24 plots the sine of both $\theta_{\nabla\widetilde{Y}_{SF_6}}$ and $\theta_{\overline{u_i''}}$. From this figure, it is clear that the turbulent species flux does not follow the mean gradient for most of the problem evolution. On the other hand, by also plotting the sine of $\theta_{\overline{u_i''}}$, it is observed that the turbulent species flux seems to align very closely with the mass-flux velocity vector. Indeed, such a result might suggest that those models which accurately solve for the mass-flux velocity could exploit this feature to obtain a better closure than gradient diffusion. Consider the following relationships:

$$\overline{\rho u_i'' Y_\alpha''} = \overline{\rho u_i Y_\alpha} - \frac{\left(\overline{\rho u_i}\right)\left(\overline{\rho Y_\alpha}\right)}{\overline{\rho}} \tag{30}$$

$$\left(\overline{\rho}\widetilde{Y}_\alpha\right)\overline{u_i''} = \left(\overline{\rho Y_\alpha}\right)\overline{u}_i - \frac{\left(\overline{\rho u_i}\right)\left(\overline{\rho Y_\alpha}\right)}{\overline{\rho}} \tag{31}$$

where we have used

$$\overline{u_i''} = \overline{u}_i - \frac{\overline{\rho u_i}}{\overline{\rho}} \tag{32}$$

Subtracting Eq. (31) from Eq. (30) gives the following exact result:

$$\begin{aligned}\overline{\rho u_i'' Y_\alpha''} - \left(\overline{\rho}\widetilde{Y}_\alpha\right)\overline{u_i''} &= \overline{\rho u_i Y_\alpha} - \left(\overline{\rho Y_\alpha}\right)\overline{u}_i \\ &= \overline{\left(\rho Y_\alpha\right) u_i'} \\ &= \left(\overline{u_i' Y_\alpha'}\right)\overline{\rho} + \left(\overline{u_i'\rho'}\right)\overline{Y}_\alpha + \overline{u_i'\rho' Y_\alpha'}\end{aligned} \tag{33}$$

Next, let us make three simplifying assumptions. First, we will neglect the triple correlation term in Eq. (33). Secondly, we will assume $\left(\overline{u_i' Y_\alpha'}\right)\overline{\rho} \approx C_t \left(\overline{u_i'\rho'}\right)\overline{Y}_\alpha$ for some constant C_t. Finally, let us assume $\overline{Y}_\alpha \approx \widetilde{Y}_\alpha$. In general, we might expect these assumptions to be valid when the velocity-density correlation is greater than the density variance or, in other words, when species diffusion more closely tracks the mean velocity field than the mean scalar field. For the shock-jet problem and potentially other problems of multi-fluid mixing, this seems to be the case for early time evolution when the turbulent Reynolds number is small and mixing is dominated by large-scale swirling rather than by small-scale mixing. When these assumptions are made, Eq. (33) can be reduced to a form that lends itself nicely for use by a turbulence model that can accurately predict the mass-flux velocity.

$$\overline{\rho u_i'' Y_\alpha''} \approx C_t \left(\overline{\rho}\widetilde{Y}_\alpha\right)\overline{u_i''} \tag{34}$$

Figures 25 and 26 plot contours of the exact turbulent species flux term as well as the proposed closure term extracted from the ensemble LES database for C_t = -2. These figures show that the proposed closure gives good qualitative and quantitative representation of the turbulent species flux until approximately 560 μs. Beyond this time, the flow is seen to become more turbulent, and the proposed closure is observed to provide poorer prediction in regions of fine-scale mixing. Of course, it is worth noting that C_t = -2 is chosen empirically based on the available LES database, and it is unlikely to be universal for all flows.

By utilizing the LES database, it is further possible to analyze the appropriateness of the three assumptions that went into constructing the proposed closure. First, in Fig. 27, contours are plotted of both Reynolds-averaged and Favre-averaged SF_6 mass fraction. Qualitatively, there is very little difference between the two until perhaps around 560 μs, where the Favre-averaged contours appear to have slightly greater magnitude in regions of fine-scale mixing. Otherwise, this plot seems to confirm that $\overline{Y}_{SF_6} \approx \widetilde{Y}_{SF_6}$ is a reasonable assumption to make for this flow. Figures 28 and 29 go on to plot the three components of Eq. (33) for both the streamwise and stream-normal components of the turbulent species flux. These plots indicate that for the early-time evolution of the cylinder, $\left(\overline{u_i' Y_\alpha'}\right)\overline{\rho} \approx 2\left(\overline{u_i'\rho'}\right)\overline{Y}_\alpha$ and $\left(\overline{u_i' Y_\alpha'}\right)\overline{\rho} \geq 5\overline{u_i'\rho' Y_\alpha'}$. However, the appropriateness of the closure assumptions is seen to diminish with time as the magnitude of the triple correlation increases. The application of the proposed closure is therefore confirmed to be limited to the early-time, low-Reynolds-number mixing. Additionally, proper application of such a closure in a RANS model presupposes a reasonable prediction of the mass-flux velocity. Such an assumption could not be made of the *k-L* model. For instance, if a gradient-diffusion assumption were made to close the mass-flux velocity (as the *k-L* model makes in its closure of the pressure work term in the *k* equation), Eq. (34) would reduce to a form that looked very much like the standard gradient diffusion closure given in Eq. (29) but with the gradient of the mean density field. Instead, the proposed closure would be best coupled with a RANS model that solves a transport equation for the mass-flux velocity, and additional work would be required to perhaps develop a model that could transition from this closure over to a standard gradient diffusion closure at higher Reynolds number.

5 Conclusions and Future Work

The present work has attempted to utilize careful application of two-dimensional LES to assess the performance of the *k-L* RANS model in an unsteady problem of turbulent mixing. A detailed grid convergence study was first performed to establish confidence in baseline LES results. This study demonstrated that reasonable convergence behavior could be obtained in high-order measures of turbulence including total mixing rate and enstrophy and that the present results compared favorably with previous computational work [14] and experimental measurements [13]. Although the present simulations were seen to converge to a different mixing rate at early time, the impact of this result on the scalar field appears to be minimal.

Then, by running a large number of two-dimensional LES realizations with multimode perturbations in the initial conditions, turbulent statistics and mean flowfields were extracted as a measure by which to evaluate the RANS model performance. Although it is acknowledged that statistics gathered in this way are expected to be contaminated by a lack of turbulent fluctuations in the spanwise *z* dimension, such fluctuations are anticipated to be small relative to fluctuations in the other two dimensions during early-time evolution, and we have therefore limited our analysis to this time period. By extracting Reynolds stresses from the LES database, it was observed that τ_{11}/τ_{22} anisotropy seemed to be mostly localized to the vortex cores and the interior re-

gion of right-left vortex interaction. Extraction of the turbulent species flux terms from the LES database revealed that turbulent diffusion does not appear to follow the mean scalar field during early time evolution, calling into question the validity of a gradient diffusion closure for these terms in RANS models during this period.

Next, a series of unsteady RANS simulations were run with two different coefficient sets and two different initialization strategies. In nearly all cases, the RANS results were observed to over-predict total mixing. Although a new coefficient set was derived that ultimately led to simulations with less turbulent mixing, a particular sensitivity to the time at which the turbulent lengthscale, L, was resolved on the mesh led to observations of non-convergence in simulations with initially unresolved L_0. Improvements that were observed with the new coefficient set in this regard were generally offset by worse prediction of k. It is therefore hypothesized that assumptions of homogeneity of turbulence that are built into the k-L turbulence closures are particularly inaccurate for the early time evolution.

Finally, a new RANS closure is proposed to better capture the early time turbulent species flux when the turbulent Reynolds number is small and the mixing is dominated by the large scales. Utilizing the LES database to assess this closure, it is shown to reasonably accurately reproduce the turbulent species flux up until about 560 μs, after which the smaller scales of turbulence begin to dominate the mixing, and the assumptions that went into the closure approximation become less accurate.

Of course, much work remains to be done to validate the proposed closure as a useful tool for RANS simulation of low-Reynolds number mixing. For one, its formulation presupposes a reasonably accurate prediction of the mass-flux velocity. It, therefore, would not integrate well into the k-L turbulence model. Additionally, it is only expected to provide benefit over the standard gradient diffusion closure during the early time mixing phase. For simulations that must cover a large range of turbulent Reynolds numbers, further work is required to integrate the proposed closure in such a way that it might perhaps transition to a more appropriate closure at later time.

Acknowledgements The authors would like to specifically acknowledge and thank Bob Tipton for his input and notes regarding the similarity analysis contained in Appendix B [50]. The authors would also like to thank Britton Olson, Mike Wickett, Oleg Schilling, Andy Cook, Bill Cabot, Mark Ulitsky, Bryan Johnson, Ivan Otero, Frank Graziani, Rob Rieben, and Brian Pudliner for their helpful input and support in the preparation of the present work.

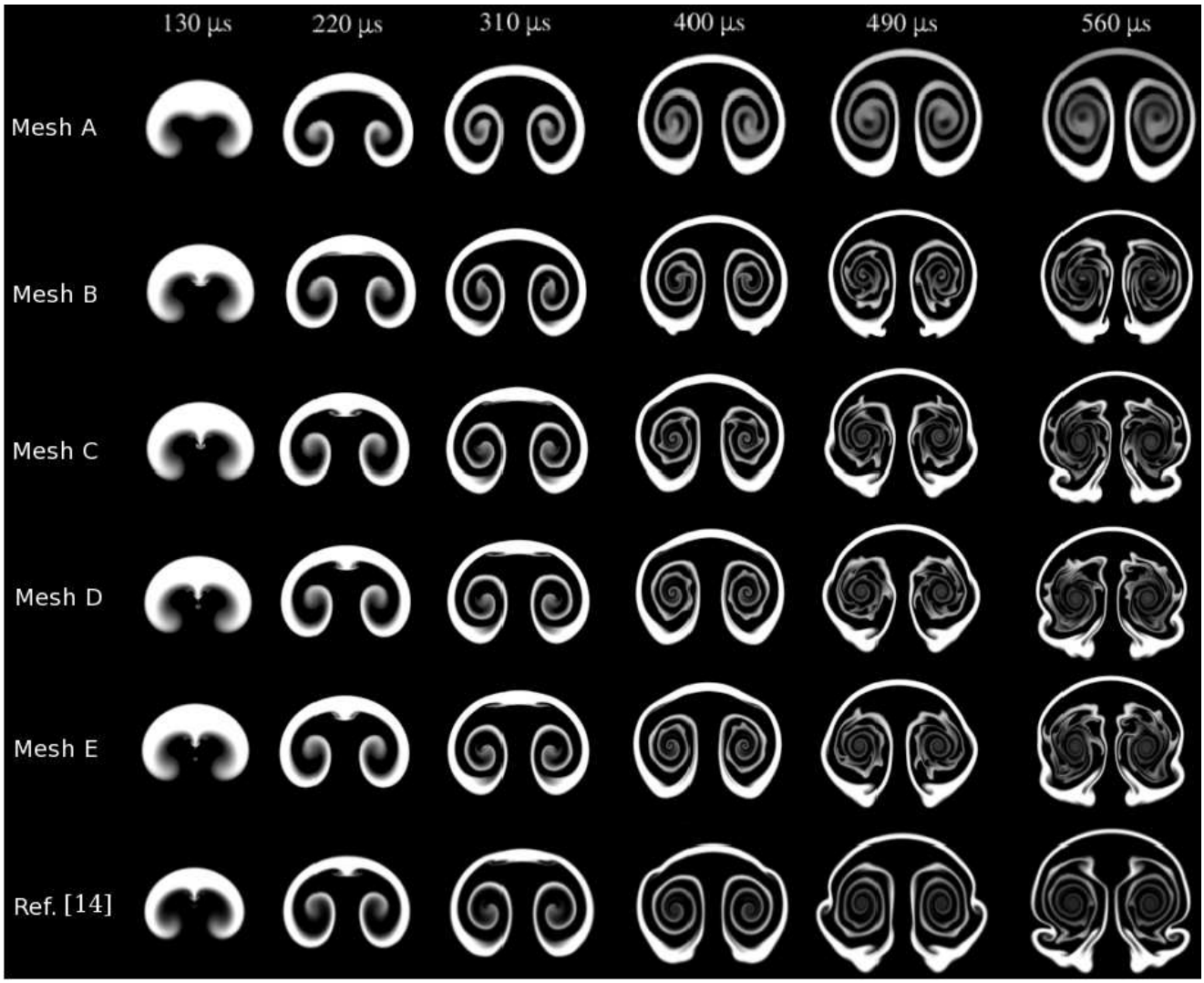

Fig. 2 Mesh resolution study: SF_6 mass fraction contours obtained from LES with no initial perturbation. Contours plotted from Y_{SF_6} = 0.1 (black) to 0.6 (white).

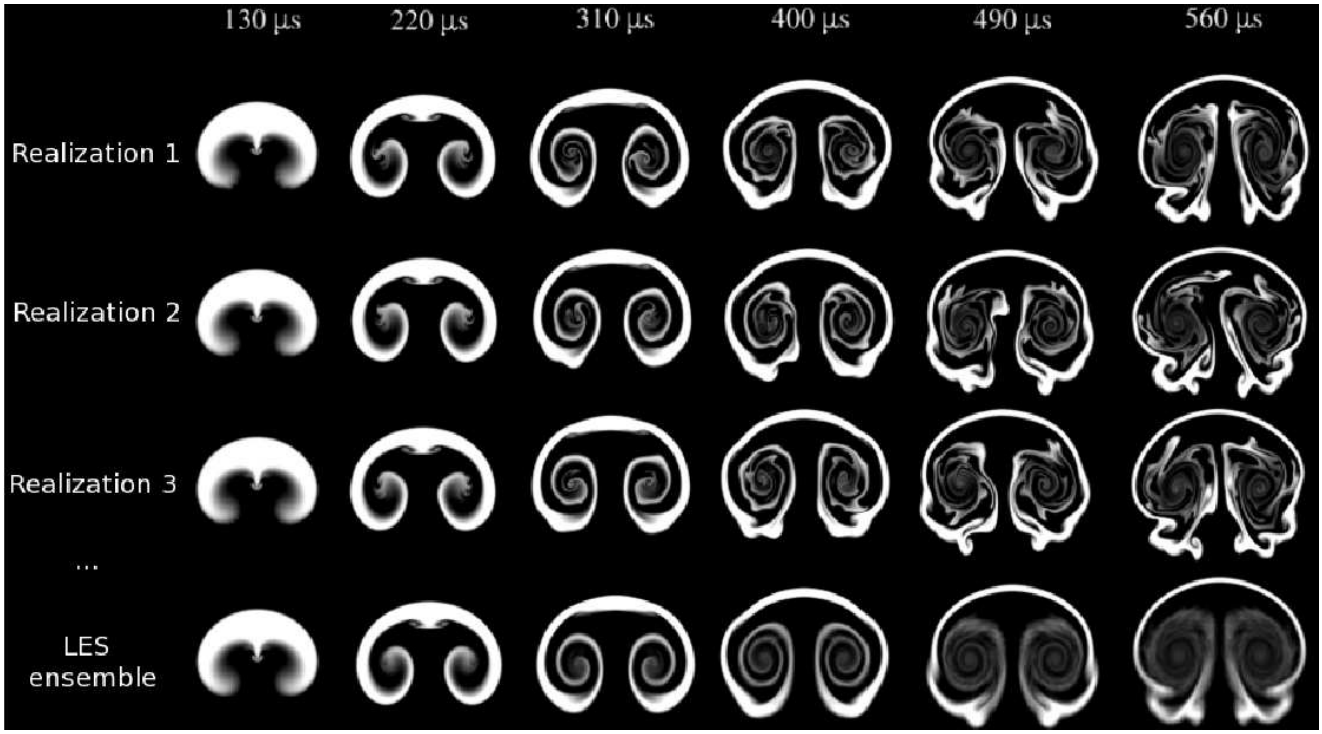

Fig. 6 Effect of initial conditions: SF_6 mass fraction contours obtained from three realizations with perturbed initial conditions and ensemble-averaged contours computed from all 20 realizations. Contours plotted from Y_{SF_6} = 0.1 (black) to 0.6 (white).

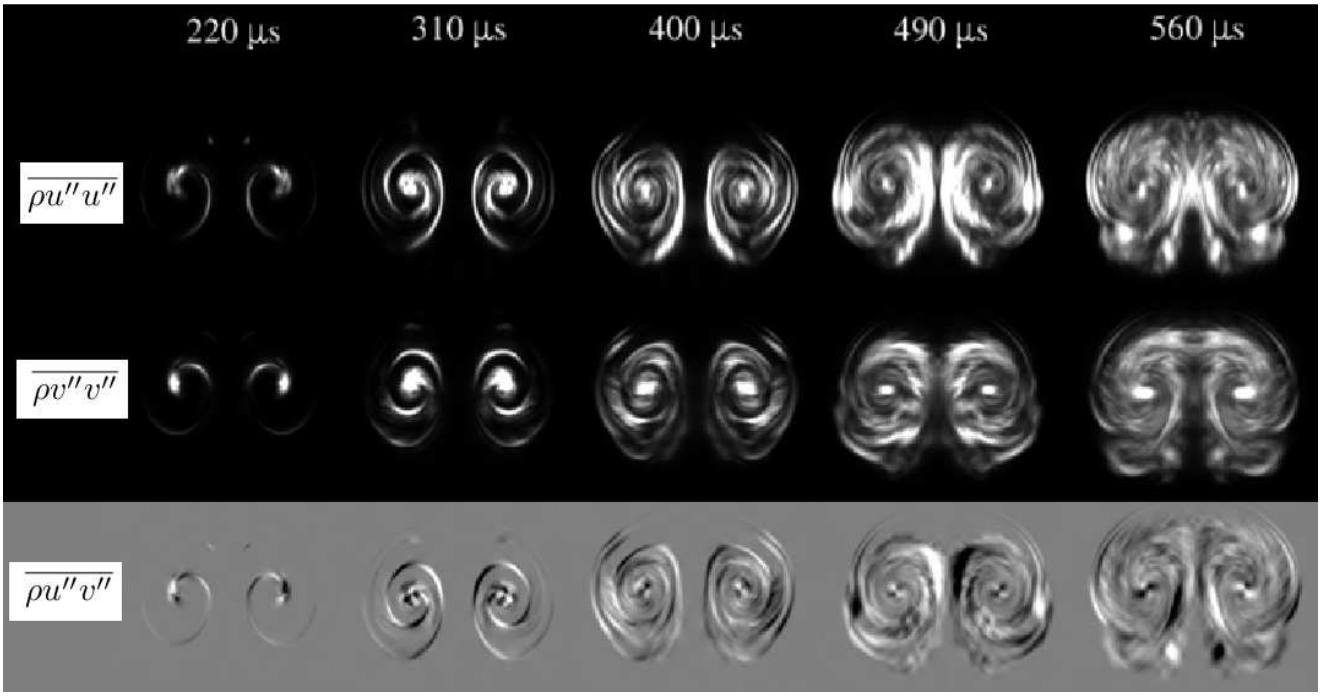

Fig. 9 Reynolds stress components computed from an ensemble of LES realizations. Contours of $\overline{\rho u'' u''}$ and $\overline{\rho v'' v''}$ plotted from 0.0 (black) to 3.0e-10 g/cm·μs^2 (white). Contours of $\overline{\rho u'' v''}$ plotted from -1.5e-10 (black) to 1.5e-10 g/cm·μs^2 (white).

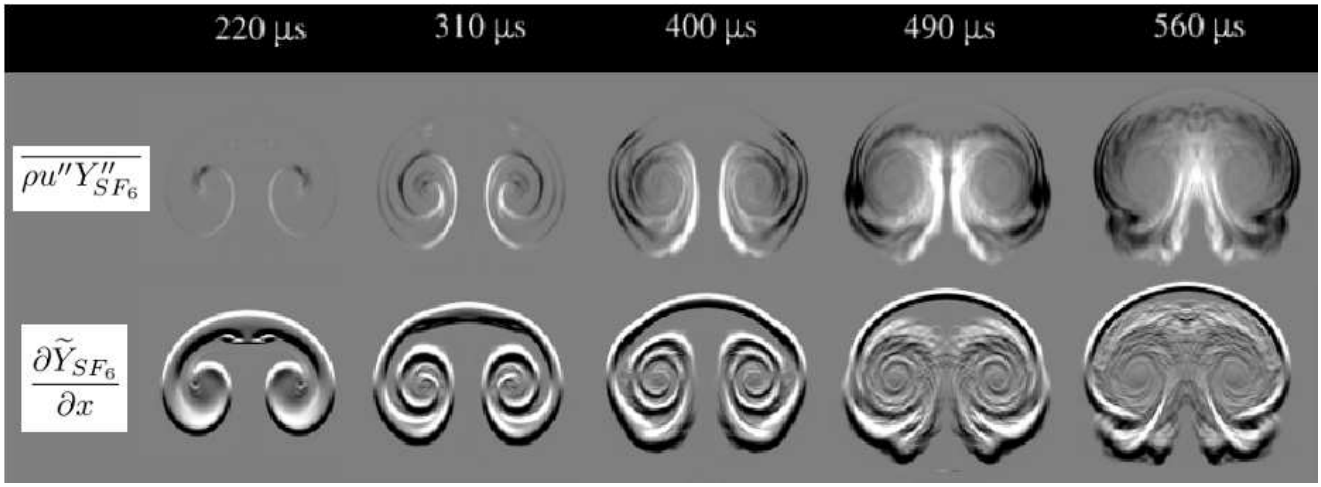

Fig. 10 Top row: Streamwise turbulent species flux component computed from an ensemble of LES realizations. Contours plotted from -1.5e-7 (black) to 1.5e-7 g/cm$^2 \cdot \mu$s (white). Bottom row: Mean streamwise scalar gradient. Contours plotted from -10.0 (black) to 10.0 cm^{-1} (white).

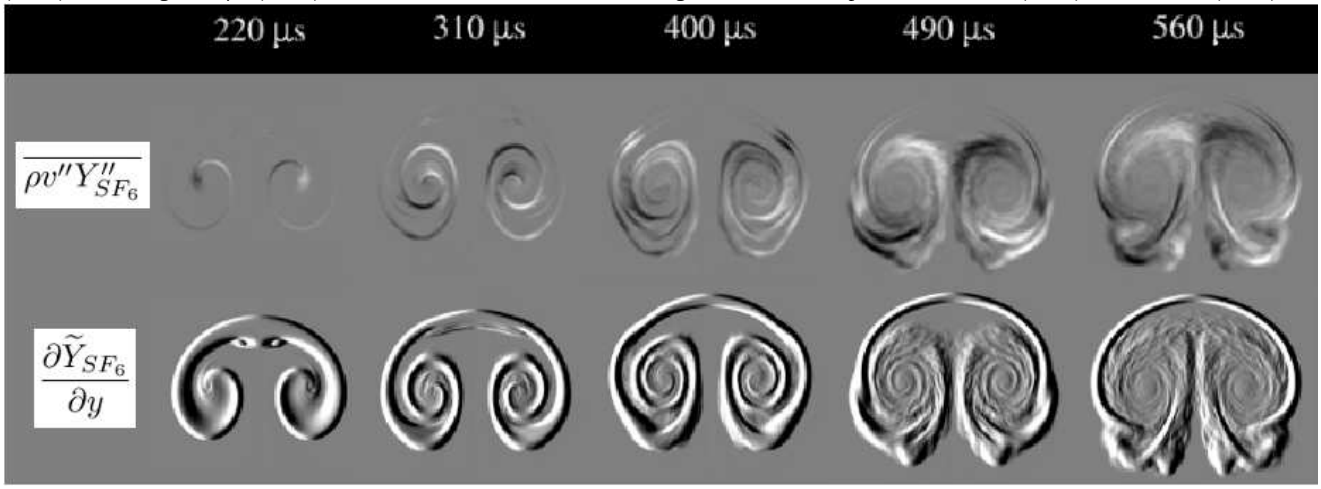

Fig. 11 Top row: Stream-normal turbulent species flux component computed from an ensemble of LES realizations. Contours plotted from -1.5e-7 (black) to 1.5e-7 g/cm$^2 \cdot \mu$s (white). Bottom row: Mean stream-normal scalar gradient. Contours plotted from -10.0 (black) to 10.0 cm^{-1} (white).

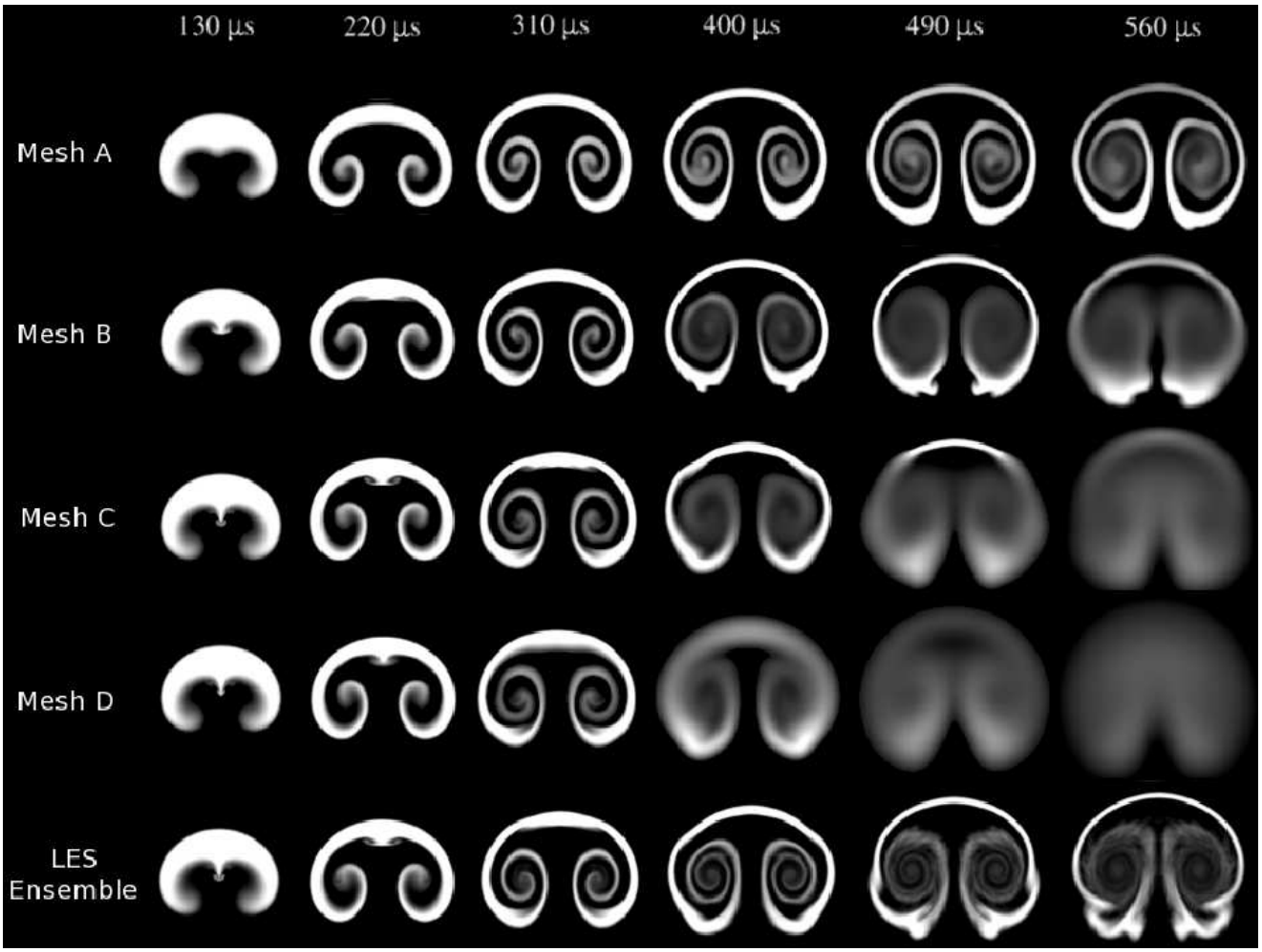

Fig. 12 Mesh resolution study: SF_6 mass fraction contours obtained with *k-L* standard coefficient set and constant $L_0 = 0.01\mu m$. Contours plotted from $\tilde{Y}_{SF_6}$ = 0.1 (black) to 0.6 (white).

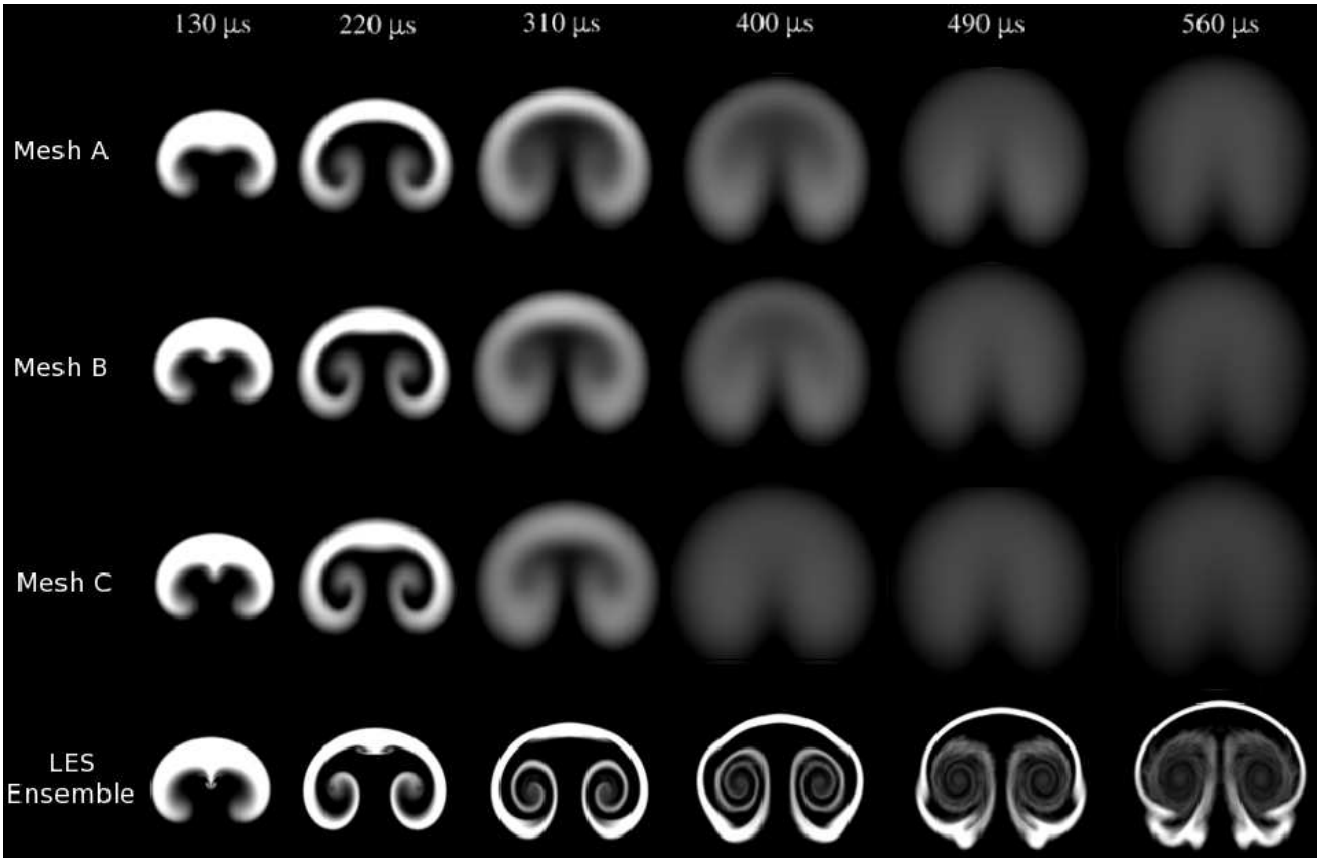

Fig. 13 Mesh resolution study: SF_6 mass fraction contours obtained with *k-L* standard coefficient set and mesh-dependent $L_0 = \Delta/2$. Contours plotted from $\widetilde{Y}_{SF_6}$ = 0.1 (black) to 0.6 (white).

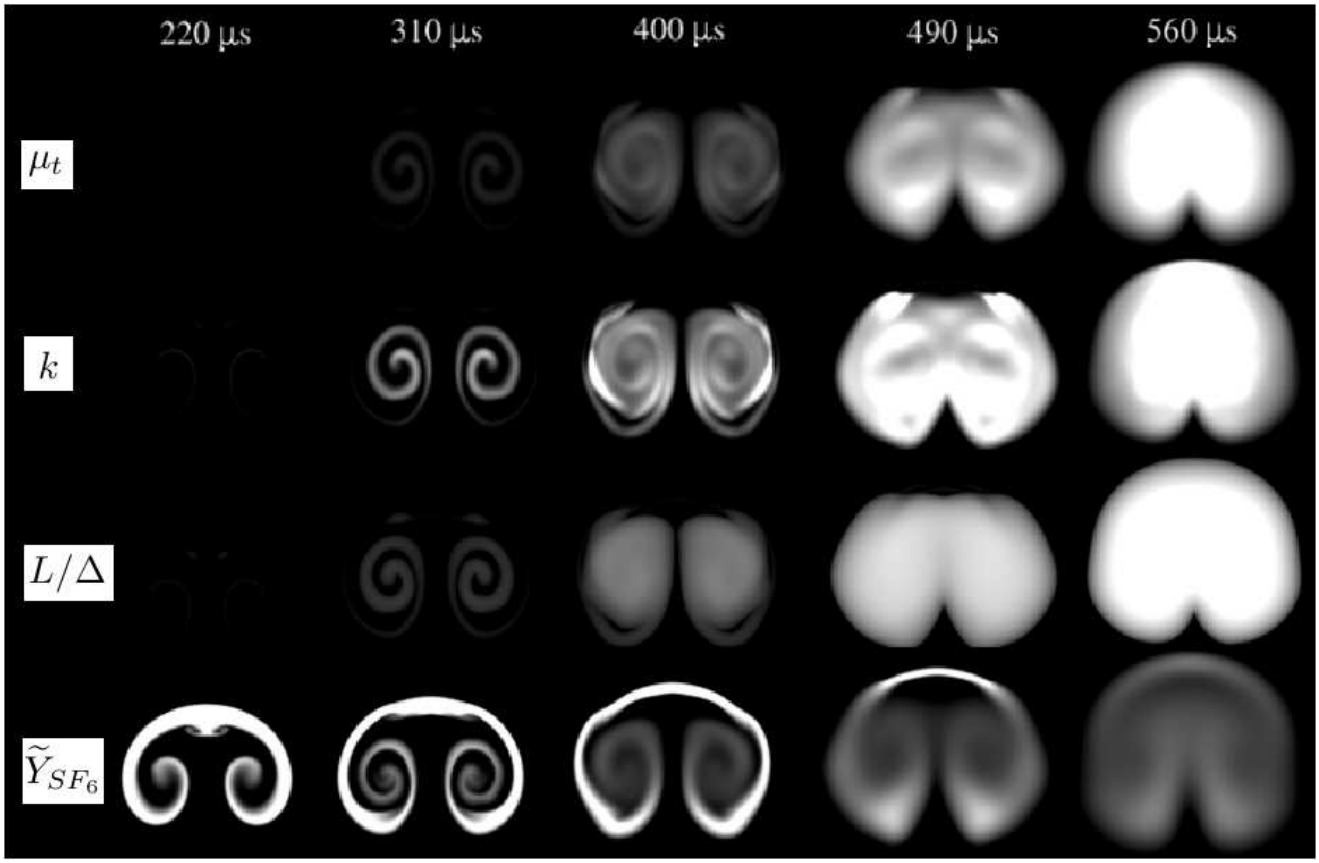

Fig. 17 Growth of turbulence parameters in *k-L* simulation with standard coefficient set and $L_0 = 0.01\mu m$ on mesh C. Contours of μ_t plotted from 0.0 (black) to 1.0e-7 g/cm·μs (white). Contours of *k* plotted from 0.0 (black) to 2.0e-7 g·cm^2/μs^2(white). Contours of L/Δ plotted from 0.0 (black) to 100.0 (white). Contours of $\widetilde{Y}_{SF_6}$ plotted from 0.1 (black) to 0.6 (white).

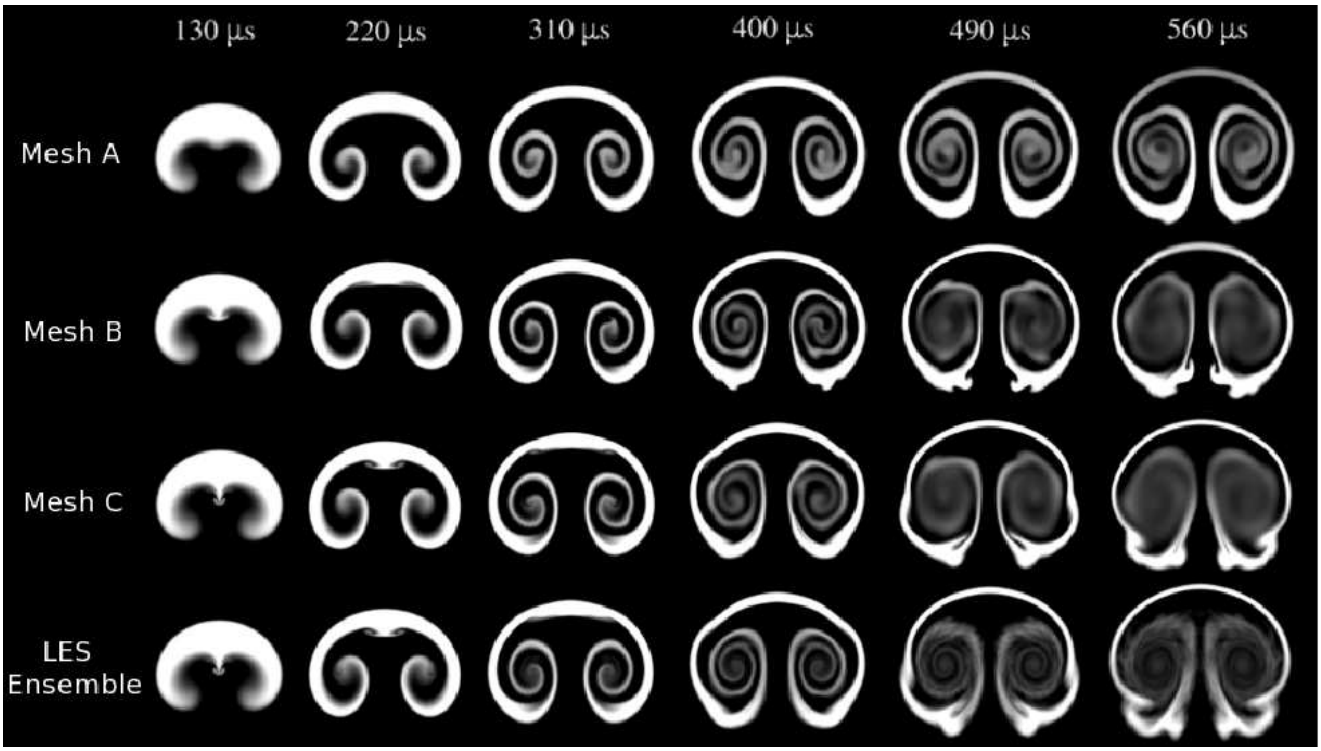

Fig. 18 Mesh resolution study: SF_6 mass fraction contours obtained with new *k-L* coefficient set and constant $L_0 = 0.01\mu m$. Contours plotted from $\widetilde{Y}_{SF_6}$ = 0.1 (black) to 0.6 (white).

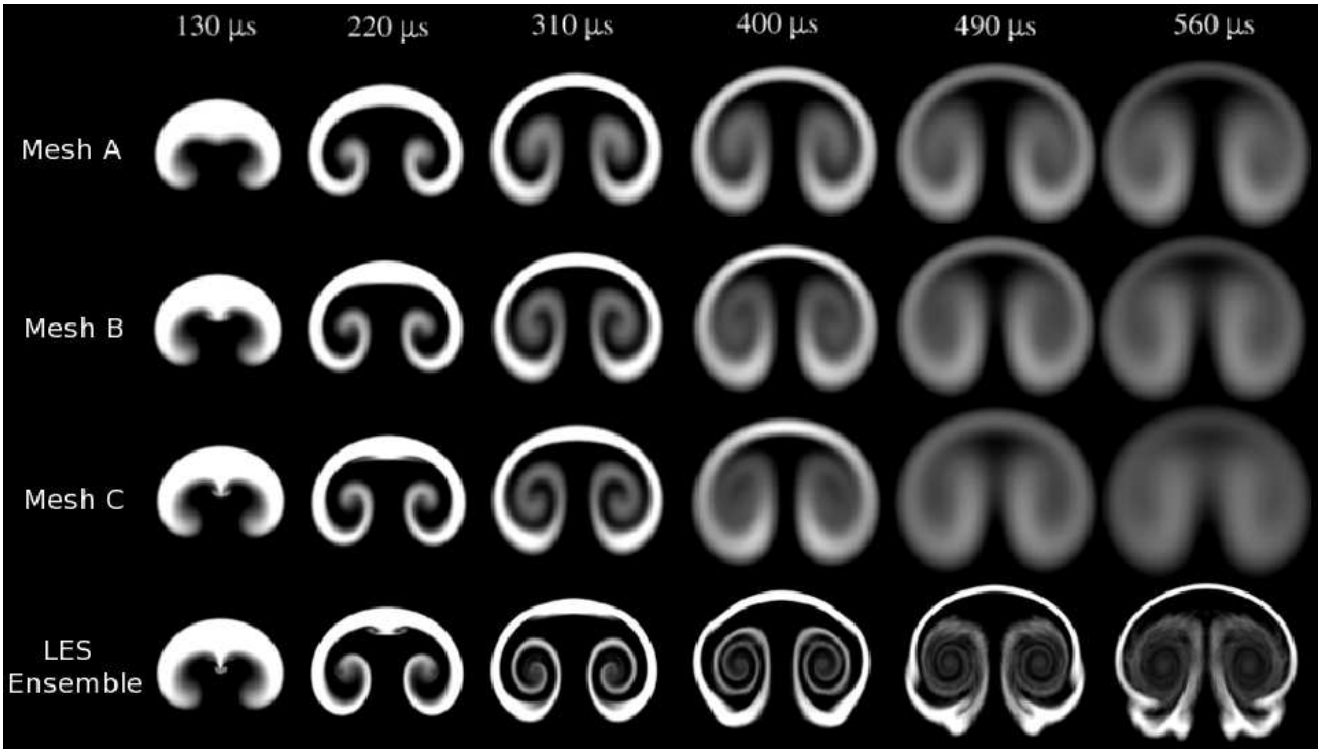

Fig. 19 Mesh resolution study: SF_6 mass fraction contours obtained with new *k-L* coefficient set and mesh-dependent $L_0 = \Delta/2$. Contours plotted from $\widetilde{Y}_{SF_6}$ = 0.1 (black) to 0.6 (white).

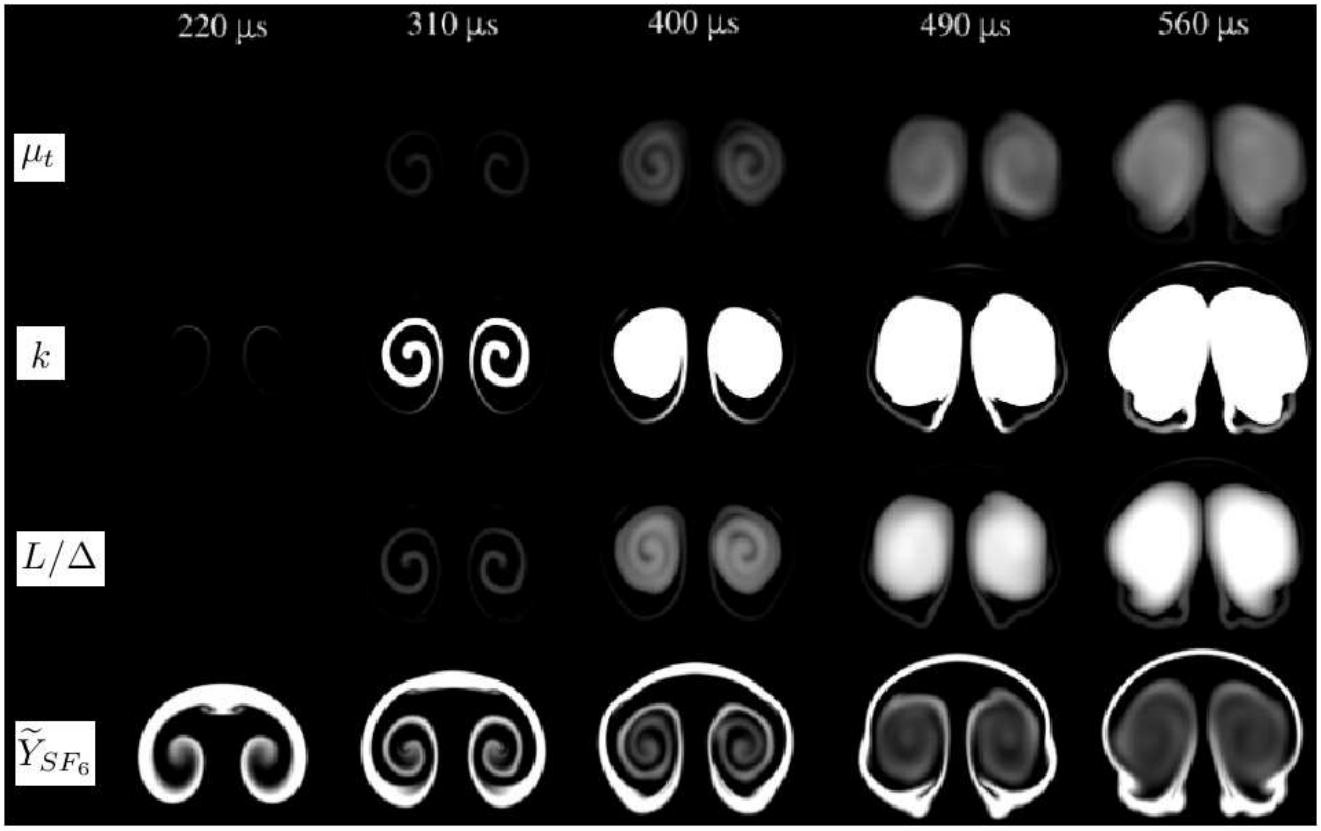

Fig. 21 Growth of turbulence parameters in *k-L* simulation with new coefficient set and $L_0 = 0.01\mu m$ on mesh C. Contours of μ_t plotted from 0.0 (black) to 1.0e-7 g/cm·μs (white). Contours of *k* plotted from 0.0 (black) to 2.0e-7 g·cm^2/μs^2(white). Contours of L/Δ plotted from 0.0 (black) to 100.0 (white). Contours of $\widetilde{Y}_{SF_6}$ plotted from 0.1 (black) to 0.6 (white).

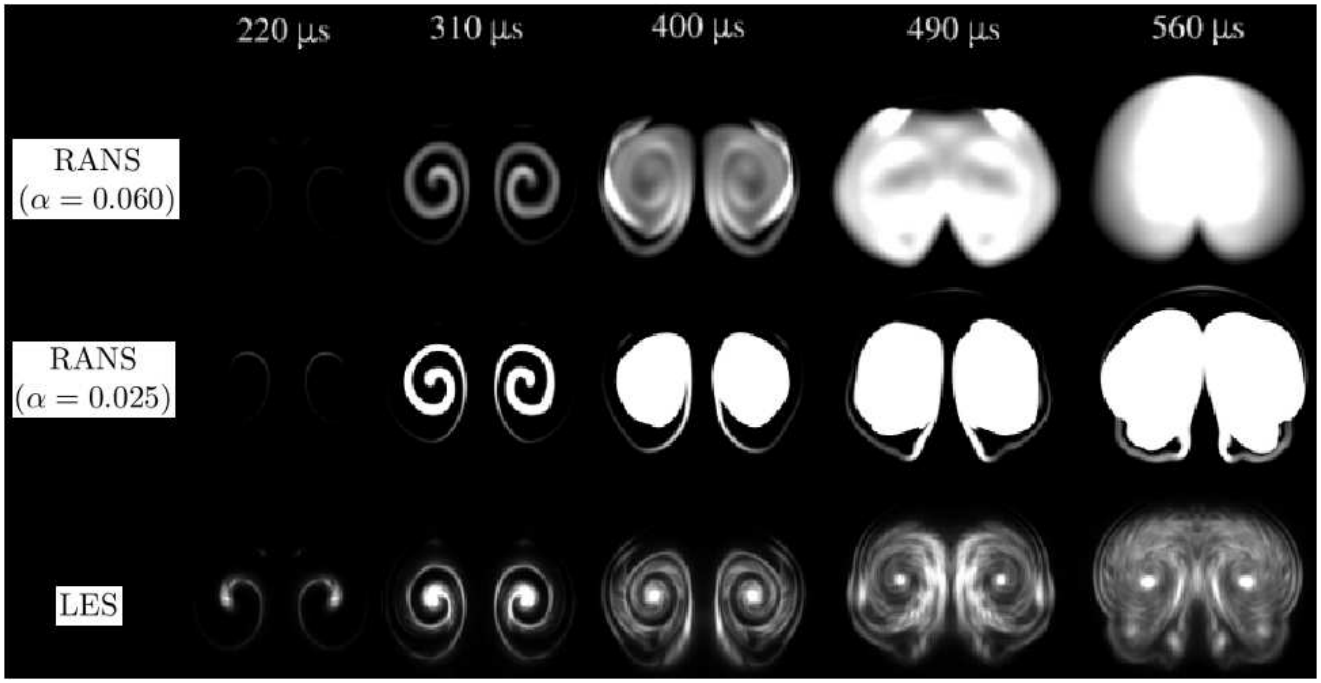

Fig. 22 A comparison of turbulence kinetic energy predicted by three approaches. RANS results taken from simulations on mesh C with $L_0 = 0.01\mu m$ using standard (top) and new (middle) coefficient sets. Contours of *k* plotted from 0.0 (black) to 2.0e-7 g·cm^2/μs^2(white).

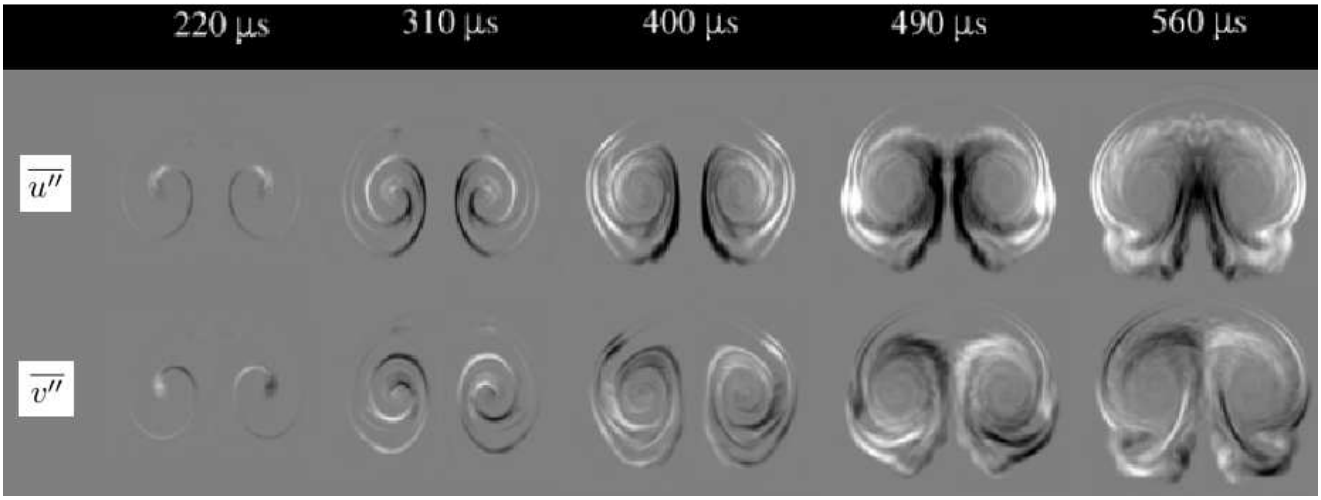

Fig. 23 Mass-flux velocities computed from an ensemble of LES realizations. Contours plotted from -1.0e-4 (black) to 1.0e-4 cm/μs (white).

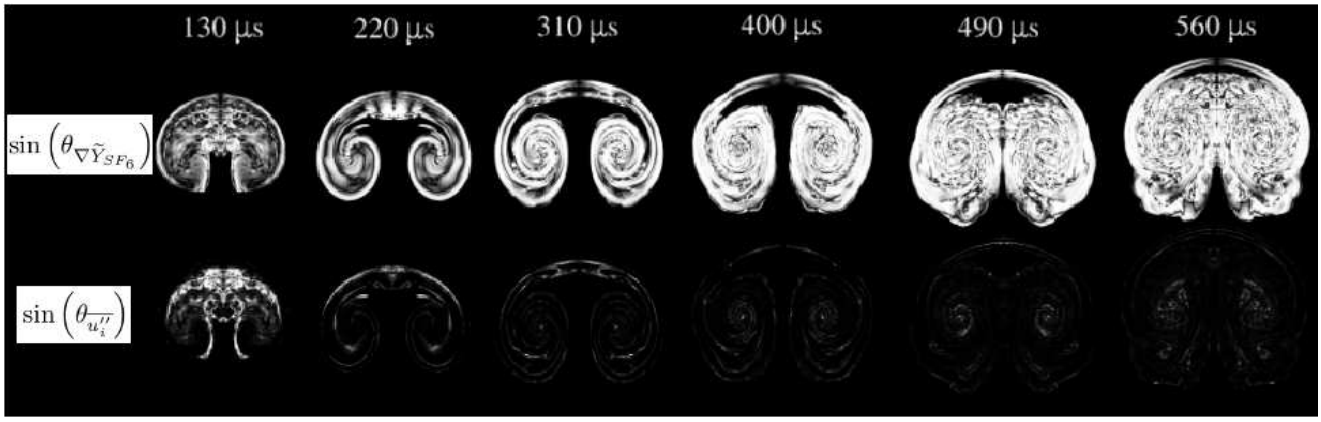

Fig. 24 Relative orientation of the turbulent species flux vector with the mean gradient vector (top row) and the mass-flux velocity vector (bottom row) extracted from an ensemble of LES realizations. Contours plotted from 0 (black) to 1 (white).

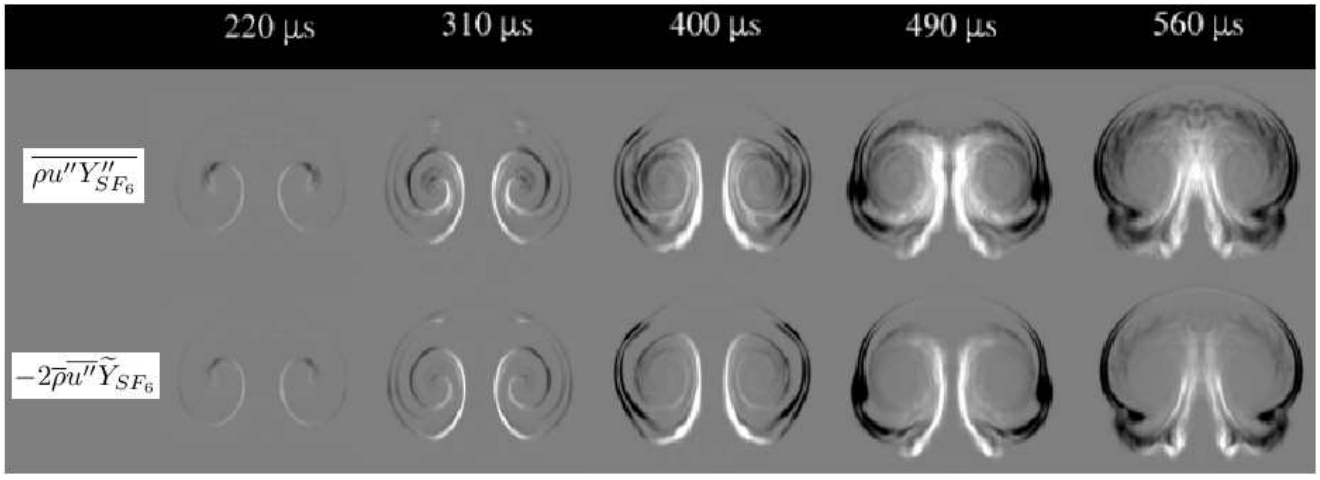

Fig. 25 Proposed closure for streamwise turbulent species flux computed from an ensemble of LES realizations. Contours plotted from -1.5e-7 (black) to 1.5e-7 g/cm$^2 \cdot \mu$s (white).

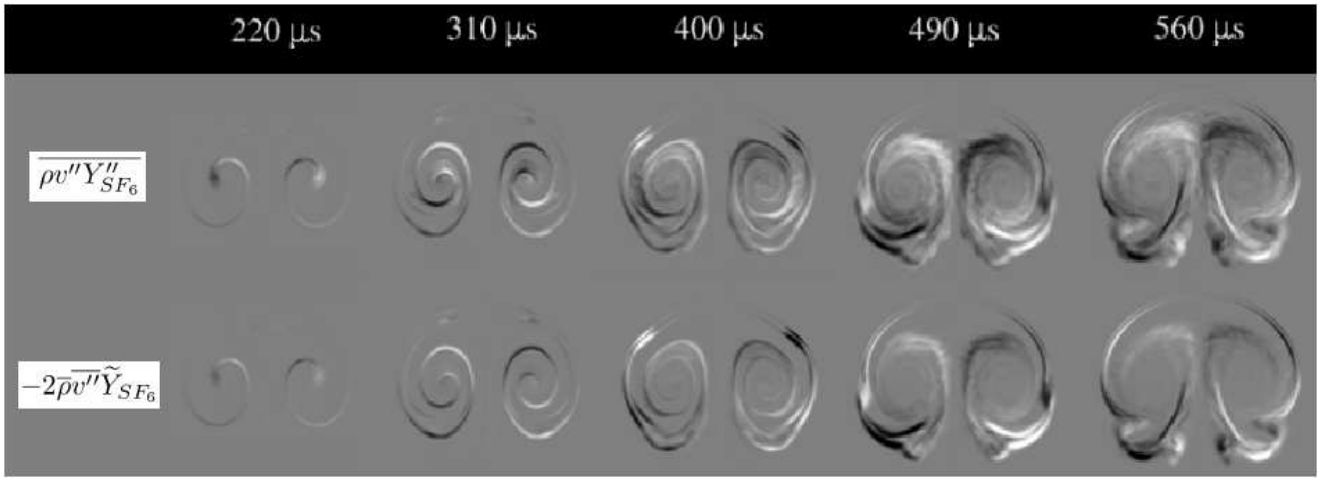

Fig. 26 Proposed closure for stream-normal turbulent species flux computed from an ensemble of LES realizations. Contours plotted from -1.5e-7 (black) to 1.5e-7 g/cm$^2 \cdot \mu$s (white).

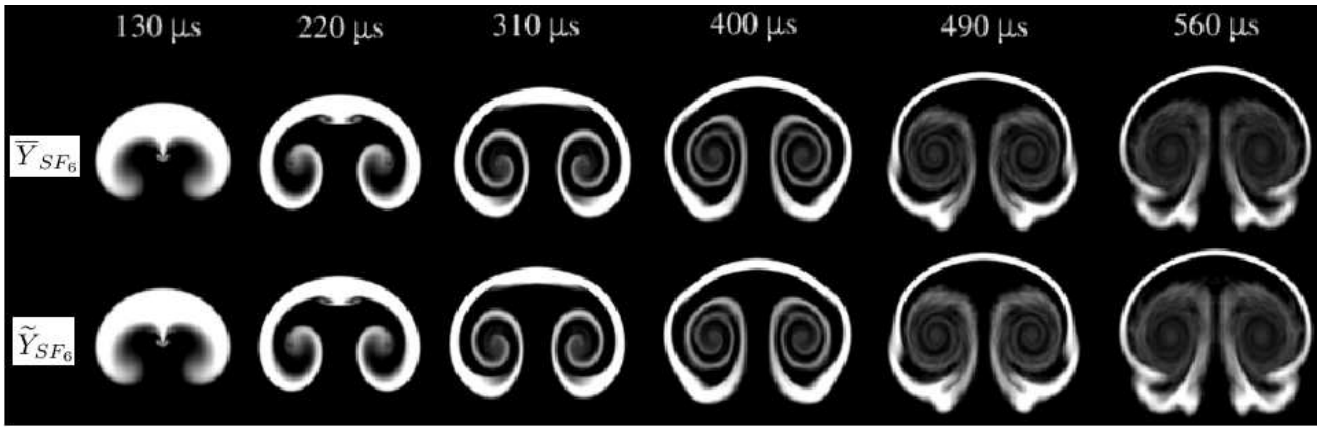

Fig. 27 Mean SF_6 mass fraction contours obtained from an ensemble of LES realizations. Top row: Reynolds averaged profiles. Bottom row: Favre averaged profiles. Contours plotted from 0.1 (black) to 0.6 (white).

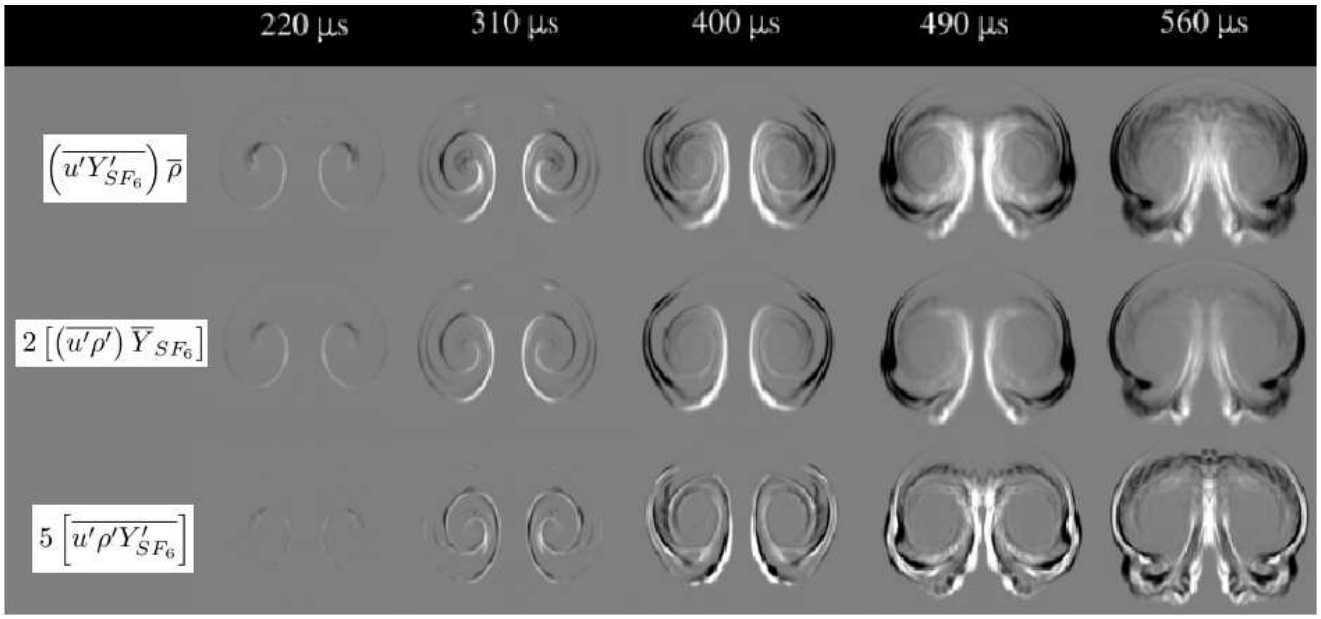

Fig. 28 Relative magnitude of three components of streamwise turbulent species flux identified in Eq. (33). Contours plotted from -1.5e-7 (black) to 1.5e-7 g/cm$^2 \cdot \mu$s (white).

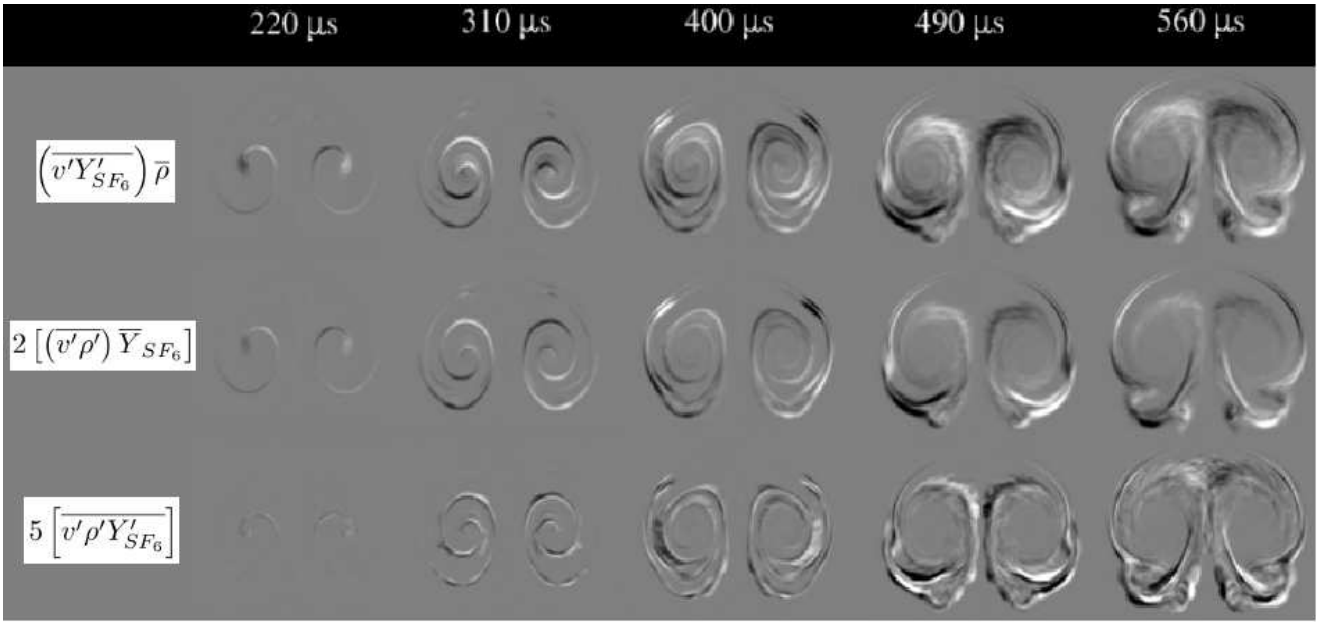

Fig. 29 Relative magnitude of three components of stream-normal turbulent species flux identified in Eq. (33). Contours plotted from -1.5e-7 (black) to 1.5e-7 g/cm$^2 \cdot \mu$s (white).

A Molecular Transport Properties

The Chapman-Enskog method [22] is a reduction of kinetic theory for use in continuum flows. Utilizing this approach, the viscosity of a single fluid component is given by Eq. (35) in terms of a collision diameter σ_α and a collision integral $\Omega_{\mu,\alpha}$. In this section, we additionally introduce the notation v_α, W_α, and z_α to indicate, respectively, the volume fraction, molar weight, and mole fraction of a single component α.

$$\mu_\alpha = \frac{26.69\times10^{-6}}{\Omega_{\mu,\alpha}}\frac{\sqrt{W_\alpha T}}{\sigma_\alpha^2} \tag{35}$$

The collision integral for viscosity is given by Eq. (36) in terms of the non-dimensional temperature, $T_\alpha^* = T/T_{\varepsilon,\alpha}$, where $T_{\varepsilon,\alpha}$ is the effective temperature characteristic of the force potential function. In this equation, A = 1.16145, B = 0.14874, C = 0.52487, D = 0.77320, E = 2.16178, and F = 2.43787.

$$\Omega_{\mu,\alpha} = A(T_\alpha^*)^{-B} + C\exp(-DT_\alpha^*) + E\exp(-FT_\alpha^*) \tag{36}$$

The thermal conductivity of a species is then related to the viscosity through the Prandtl number, where Pr=0.72.

$$\kappa_\alpha = \frac{C_{p,\alpha}\mu_\alpha}{\mathrm{Pr}} \tag{37}$$

Next, the Wilke rule with Herning and Zipperer approximation [23] is utilized to form a mixture viscosity and thermal conductivity. This rule, which is written in general form for some quantity ξ, is given by equation 38.

$$\xi = \frac{\sum_{\alpha=1}^{N}\xi_\alpha Y_\alpha/W_\alpha^{1/2}}{\sum_{\alpha=1}^{N}Y_\alpha/W_\alpha^{1/2}} \tag{38}$$

Mass diffusivity coefficients are obtained in a similar manner. The Chapman-Enskog expression for the diffusion coefficient of one component into another is given by Eq. (39). In this equation, average molar weights and collision diameters are given by $W_{\alpha\beta} = 2/(W_\alpha^{-1}+W_\beta^{-1})$ and $\sigma_{\alpha\beta} = (\sigma_\alpha+\sigma_\beta)/2$, respectively.

$$D_{\alpha\beta} = \frac{0.00266}{\Omega_{D,\alpha\beta}}\frac{T^{3/2}}{p\sqrt{W_{\alpha\beta}}\left(\sigma_{\alpha\beta}\right)^2} \tag{39}$$

The collision integral for diffusivity is then given by Eq. (40) in terms of the non-dimensional temperature, $T_{\alpha\beta}^* = T/T_{\varepsilon,\alpha\beta}$, where $T_{\varepsilon,\alpha\beta} = \sqrt{T_{\varepsilon,\alpha}T_{\varepsilon,\beta}}$ In this equation, A = 1.06036, B = 0.15610, C = 0.19300, D = 0.47635, E = 1.03587, F = 1.52996, G = 1.76474, and H = 3.89411.

$$\begin{aligned}\Omega_{D,\alpha\beta} =& A(T_{\alpha\beta}^*)^{-B} + C\exp(-DT_{\alpha\beta}^*) + \\ & E\exp(-FT_{\alpha\beta}^*) + G\exp(-HT_{\alpha\beta}^*)\end{aligned} \tag{40}$$

The Ramshaw method [24] is then utilized to provide effective binary diffusivities. This method, which is given by Eq. (41), ensures that all diffusive mass fluxes sum to zero.

$$D_\alpha = (1-z_\alpha)\left(\sum_{\alpha\neq\beta}^{N} z_\beta/D_{\alpha\beta}\right)^{-1} \tag{41}$$

Table 3 summarizes the constants used in Eqs. (35) through (41). Air is assumed to be a mixture of 79% N_2 and 21% O_2 (by molar ratio).

Table 3 Constants used for computing molecular transport properties

Constant	N_2	O_2	SF_6
$T_{\varepsilon,\alpha}$	82.0	102.6	212.0
σ_α	3.7380	3.4800	5.1990
W_α	28.0	32.0	148.0
γ_α	1.4	1.4	1.09

B Derivation of a New k-L Coefficient Set

In the original derivation of the Dimonte and Tipton k-L model, similarity analysis was used to derive a self-consistent set of model constants [20,50]. Here, the same analysis is applied, allowing for two additional degrees of freedom ($C_L \neq 1$ and $N_k \neq 1$).

Self-Similarity of the L Equation

The L transport equation in one dimension is given by:

$$\rho\frac{DL}{Dt} = \frac{\partial}{\partial x}\left(\frac{\mu_t}{N_L}\frac{\partial L}{\partial x}\right) + C_L\rho\sqrt{2k} + C_c\rho L\frac{\partial u}{\partial x} \tag{42}$$

where the turbulent viscosity is given by

$$\mu_t = \rho C_\mu L\sqrt{2k} \tag{43}$$

Consider a change of variable in terms of the self-similar mixing width, $h(t)$.

$$\chi \equiv \frac{x}{h} \tag{44}$$

It is then assumed that the analytic functions k and L are separable in space and time:

$$k(\chi,t) = K_0(t)\,f(\chi) \tag{45a}$$
$$L(\chi,t) = L_0(t)\,f^{1/2}(\chi) \tag{45b}$$

Assuming incompressibility and an Atwood number that approaches zero allows us to cancel ρ and drop spatial derivatives of velocity. Plugging Eqs. (43) through (45) into Eq. (42) then gives:

$$\begin{aligned}\frac{D}{Dt}\left(L_0 f^{1/2}\right) =& \frac{\partial}{\partial x}\left(\frac{C_\mu}{N_L}L_0 f\sqrt{2K_0}\frac{\partial}{\partial x}\left(L_0 f^{1/2}\right)\right) \\ & + C_L f^{1/2}\sqrt{2K_0}\end{aligned} \tag{46}$$

We next assume that the spatial function f is self-similar according to

$$f(\chi) = 1-\chi^2 \tag{47a}$$
$$L_0(t) = \beta h(t) \tag{47b}$$

By distributing the derivatives, Eq. (46) can be reduced after a fair amount of algebra to the following form:

$$\dot{L_0} = \sqrt{2K_0}\left[C_L - \frac{C_\mu}{N_L}\beta^2\right] + \sqrt{2K_0}\left[2\frac{C_\mu}{N_L}\beta^2 - C_L\right]\left(\frac{x}{h}\right)^2 \tag{48}$$

In order to satisfy the self-similarity ansatz, we require that both the terms proportional to x^2 and the constant terms vanish. These requirements can be satisfied simultaneously with the following constraints:

$$\beta = \sqrt{\frac{C_L N_L}{2C_\mu}} \tag{49}$$

$$\dot{L}_0(t) = \frac{C_L}{2}\sqrt{2K_0} \qquad \text{(The } L_0 \text{ Equation)}$$

Self-Similarity of the k Equation

The k transport equation in one dimension is given by:

$$\begin{aligned}\rho\frac{Dk}{Dt} =& \frac{\partial}{\partial x}\left(\frac{\mu_t}{N_k}\frac{\partial k}{\partial x}\right) + \rho C_B A(x) g\sqrt{2k} \\ & - \rho C_D \frac{(2k)^{3/2}}{L} - \frac{2}{3}\rho k\frac{\partial u}{\partial x}\end{aligned} \tag{50}$$

where $A(x)$ is the k-L Atwood number:

$$A(x) = A_D + C_A\left[\frac{L}{1+\frac{L}{\rho}\left|\frac{\partial\rho}{\partial x}\right|}\right]\frac{\partial\rho}{\partial x} \tag{51}$$

Here, A_D is the discontinuous part of the Atwood number which will always vanish in the self-similar limit. In the limit of small Atwood number, the denominator of the continuous part of the Atwood number will also vanish. This means for small Atwood number and in the self-similar limit, the k-L Atwood number becomes

$$A(x) = C_A\frac{L}{\rho}\frac{\partial\rho}{\partial x} \tag{52}$$

We assume that the density gradient may be approximated in terms of the density of the light fluid, ρ_L and the density of heavy fluid, ρ_H:

$$\frac{\partial\rho}{\partial x} \approx \frac{\rho_H - \rho_L}{2h} \tag{53}$$

Plugging Eq. (53) into Eq. (52), utilizing the scaling assumption for $L_0 = \beta h$, and utilizing the small Atwood number approximation $\rho \approx (\rho_H + \rho_L)/2$, we have:

$$A(x) = \beta C_A f^{1/2}\left(\frac{\rho_H - \rho_L}{\rho_H + \rho_L}\right) \tag{54}$$

Recall the definition of the conventional Atwood number:

$$A_T = \left(\frac{\rho_H - \rho_L}{\rho_H + \rho_L}\right) \tag{55}$$

Since the self-similar function f has a maximum value of 1 at x=0, it is convenient to define the k-L Atwood number such that it has peak value equal to the conventional Atwood number at x=0. This constraint requires us to choose

$$C_A = \frac{1}{\beta} = \sqrt{\frac{2C_\mu}{C_L N_L}} \tag{56}$$

Utilizing Eq. (56) and substituting Eqs. (54) and (55) into Eq. (50) gives

$$\begin{aligned}\rho\frac{Dk}{Dt} =& \frac{\partial}{\partial x}\left(\frac{\mu_t}{N_k}\frac{\partial k}{\partial x}\right) + \rho C_B A_T g f^{1/2}\sqrt{2k} \\ & - \rho C_D\frac{(2k)^{3/2}}{L} - \frac{2}{3}\rho k\frac{\partial u}{\partial x}\end{aligned} \tag{57}$$

Utilizing incompressibility and an Atwood number that approaches zero allows us to cancel ρ and drop spatial derivatives of velocity

$$\begin{aligned}\frac{Dk}{Dt} =& \frac{\partial}{\partial x}\left(\frac{C_\mu L_0 f\sqrt{2K_0}}{N_k}\frac{\partial k}{\partial x}\right) + C_B A_T g f^{1/2}\sqrt{2k} \\ & - C_D\frac{(2k)^{3/2}}{L}\end{aligned} \tag{58}$$

After a fair amount of algebra and rearranging, we are able to derive the reduced k equation:

$$\begin{aligned}0 =& \left[\dot{K}_0 + \frac{C_L N_L}{2N_k}\frac{(2K_0)^{3/2}}{L_0} - C_B A_T g\sqrt{2K_0} + C_D\frac{(2K_0)^{3/2}}{L_0}\right] \\ & - \left[\dot{K}_0 + \left(\frac{3C_L N_L}{2N_k} - \frac{C_L}{2}\right)\frac{(2K_0)^{3/2}}{L_0} - C_B A_T g\sqrt{2K_0} + C_D\frac{(2K_0)^{3/2}}{L_0}\right]\left(\frac{x}{h}\right)^2\end{aligned} \tag{59}$$

As we did before with the L equation, in order to satisfy the self-similarity ansatz, we require both the constant terms and the terms that scale with x^2 to go to zero. This gives us our two moment equations:

$$\begin{aligned}&\dot{K}_0 + \frac{C_L N_L}{2N_k}\frac{(2K_0)^{3/2}}{L_0} - C_B A_T g\sqrt{2K_0} \\ &\quad + C_D\frac{(2K_0)^{3/2}}{L_0} = 0\end{aligned} \qquad \text{(Zero Moment)}$$

$$\begin{aligned}&\dot{K}_0 + \left(\frac{3C_L N_L}{2N_k} - \frac{C_L}{2}\right)\frac{(2K_0)^{3/2}}{L_0} \\ &\quad - C_B A_T g\sqrt{2K_0} + C_D\frac{(2K_0)^{3/2}}{L_0} = 0\end{aligned} \qquad \text{(Second Moment)}$$

Inspection of these two equations reveals that they can only both be satisfied if

$$\frac{C_L N_L}{2N_k} = \left(\frac{3C_L N_L}{2N_k} - \frac{C_L}{2}\right) \tag{60}$$

which reduces to

$$\frac{N_L}{N_k} = \frac{1}{2} \tag{61}$$

With this constraint, we can equivalently write our constraint on β as:

$$\beta = \sqrt{\frac{C_L N_L}{2C_\mu}} = \sqrt{\frac{C_L N_k}{4C_\mu}} = \frac{1}{2}\sqrt{\frac{C_L N_k}{C_\mu}} \tag{62}$$

Similarly, Eq. (61) reduces both the zero moment and the second moment to the same equation.

$$\dot{K}_0 = C_B A_T g\sqrt{2K_0} - \frac{(2K_0)^{3/2}}{L_0}\left(C_D + \frac{C_L}{4}\right) \qquad \text{(The } K_0 \text{ Equation)}$$

It is now convenient to make a change of variable $V_0 = \sqrt{2K_0}$. Then substitution into the K_0 equation gives the V_0 equation:

$$\dot{V}_0 = C_B A_T g - \frac{V_0^2}{L_0}\left(C_D + \frac{C_L}{4}\right) \qquad \text{(The } V_0 \text{ Equation)}$$

Richtmyer-Meshkov Growth Rate

We now utilize experimental observations to provide constraints on the observed coefficient set. After the shock has passed, the acceleration term in the V_0 equation will vanish, and the L_0 and V_0 equations reduce to the following:

$$\dot{L}_0 = \frac{C_L}{2} V_0 \tag{63}$$

$$\dot{V}_0 = -\frac{V_0^2}{L_0}\left(C_D + \frac{C_L}{4}\right) \tag{64}$$

Substitution of the L_0 equation into the V_0 equation gives a single equation for L_0:

$$\left(\frac{2}{C_L}\ddot{L}_0\right) = -2\frac{\dot{L}_0^2}{L_0}\left(\frac{C_D}{C_L} + \frac{1}{4}\right) \tag{65}$$

Integrating this equation for L_0 requires initial values of $L_0(0)$ and $\dot{L}_0(0)$. Anticipating the result, we try a solution of the form:

$$L_0(t) = L_0(0)\left[\frac{\dot{L}_0(0)}{\theta L_0(0)} + 1\right]^{\theta} \tag{66}$$

Plugging this equation and its derivatives into Eq. (65) reduces to:

$$\frac{\theta - 1}{\theta} = -2\left(\frac{C_D}{C_L} + \frac{1}{4}\right) \tag{67}$$

or

$$\frac{C_D}{C_L} = \frac{1-\theta}{2\theta} - \frac{1}{4} = \frac{2-3\theta}{4\theta} \tag{68}$$

Rayleigh-Taylor Growth Rate

For the case in which the acceleration term in the V_0 equation cannot be dropped, let us assume a solution of the form $L_0 = BA_T g t^2$. Substituting into the L_0 equation gives:

$$V_0 = \frac{4}{C_L} B A_T g t \tag{69}$$

Putting the trial solutions into the V_0 equation gives (after some algebra):

$$B = \frac{C_B C_L}{8\left(1 + 2\frac{C_D}{C_L}\right)} \tag{70}$$

We know for small Atwood number, the bubble height will be $h(t)$:

$$h(t) = \frac{L_0(t)}{\beta} = \sqrt{\frac{C_\mu C_L}{N_K}}\left(\frac{C_B}{4\left(1 + 2\frac{C_D}{C_L}\right)}\right) A_T g t^2 \tag{71}$$

And, we know that bubble height should grow according to $h(t) = \alpha_b g A_T t^2$. Utilizing this, we can derive the following expression for the buoyancy coefficient:

$$C_B = \frac{4\alpha_b\left(1 + 2\frac{C_D}{C_L}\right)}{\sqrt{\frac{C_\mu C_L}{N_K}}} \tag{72}$$

This makes the Rayleigh-Taylor constant B:

$$B = \frac{\alpha_b}{2}\sqrt{\frac{C_L N_K}{C_\mu}} \tag{73}$$

Another useful identity is that the ratio of K_0 to L_0 should be constant.

$$\frac{K_0}{L_0} = \frac{V_0^2}{2L_0} = 4\alpha_b A_T g\sqrt{\frac{N_K}{C_L^3 C_\mu}} \tag{74}$$

The turbulent kinetic energy generated within an RT mixing layer is given by

$$\begin{aligned} E_K &= \int_{-h}^{h} \rho K(x,t)\mathrm{d}x \\ &= K_0 \int_{-h}^{h}\left(\overline{\rho} + \frac{\partial \rho}{\partial x}x\right)\left(1 - \left(\frac{x}{h}\right)^2\right)\mathrm{d}x \\ &= K_0 \int_{-h}^{h}\left[\overline{\rho}\left(1 - \left(\frac{x}{h}\right)^2\right) + \frac{\partial \rho}{\partial x}\left(x - \frac{x^3}{h^2}\right)\right]\mathrm{d}x \end{aligned} \tag{75}$$

where

$$\overline{\rho} = \frac{\rho_H + \rho_L}{2} \tag{76a}$$

$$\frac{\partial \rho}{\partial x} = \frac{\rho_H - \rho_L}{2h} \tag{76b}$$

By symmetry, we expect the integral over odd powers of x to vanish, leaving us with:

$$E_K = \frac{4}{3} h(t)\overline{\rho} K_0(t) \tag{77}$$

Since K_0/L_0 is constant, K_0/h should also be constant.

$$\frac{K_0}{h} = \beta\frac{K_0}{L_0} = \frac{2\alpha_b A_T g N_K}{C_L C_\mu} \tag{78}$$

Utilizing this expression, we can rewrite Eq. (77) as:

$$E_K = \frac{8}{3}\left(\frac{N_K}{C_L C_\mu}\right)\alpha_b A_T \overline{\rho} g h^2 \tag{79}$$

The gravitational potential energy within the RT mixing layer can also be derived by imagining a material interface at x=0 and integrating over a distance $2d$:

$$\begin{aligned}\mathrm{PE} &= -g\int_{-d}^{d}\rho(x)x\mathrm{d}x \\ &= -g\int_{-d}^{-h}\rho_L x\mathrm{d}x - g\int_{-h}^{h}\left(\overline{\rho}+\frac{\partial\rho}{\partial x}x\right)x\mathrm{d}x - g\int_{h}^{d}\rho_H x\mathrm{d}x\end{aligned} \tag{80}$$

Again, integrals of odd powers of x vanish, leaving us with:

$$\begin{aligned}\mathrm{PE} &= -\frac{g}{2}\rho_L\left(h^2-d^2\right) - \frac{2g}{3}\frac{\partial\rho}{\partial x}h^3 - \frac{g}{2}\rho_H\left(d^2-h^2\right) \\ &= -\frac{g}{2}\left(\rho_H-\rho_L\right)d^2 + \frac{g}{6}\left(\rho_H-\rho_L\right)h^2\end{aligned} \tag{81}$$

Since we are only interested in the change in potential energy over the mixing width, we consider the term proportional to h:

$$\Delta\mathrm{PE} = \frac{g}{6}\left(\rho_H-\rho_L\right)h^2 \tag{82}$$

Thus, the fraction of potential energy converted to kinetic energy is given by:

$$\frac{E_K}{\Delta\mathrm{PE}} = \frac{\frac{8}{3}\left(\frac{N_K}{C_L C_\mu}\right)\alpha_b A_T\left(\frac{\rho_H+\rho_L}{2}\right)gh^2}{\frac{g}{6}\left(\rho_H-\rho_L\right)h^2} = \frac{8N_K\alpha_b}{C_L C_\mu} \tag{83}$$

or

$$\frac{C_\mu C_L}{N_K} = 8\alpha_b\frac{\Delta\mathrm{PE}}{E_K} \tag{84}$$

Self-Similarity of the Scalar Equation

Our conservation equation for species mass fraction in one dimension is given by Eq. (85), where without loss of generality we have neglected to write the species subscript on the mass fraction, Y_α. We have done this in order to avoid confusion with the Rayleigh-Taylor growth rate, α_b

$$\rho\frac{DY}{Dt} = \frac{\partial}{\partial x}\left(\frac{\mu_t}{N_Y}\frac{\partial Y}{\partial x}\right) \tag{85}$$

Substituting Eq. (43) and applying the incompressibility assumption reduces this equation to:

$$\frac{DY}{Dt} = \frac{\partial}{\partial x}\left(\frac{C_\mu L\sqrt{2k}}{N_Y}\frac{\partial Y}{\partial x}\right) \tag{86}$$

We assume that the self-similar solution must look like

$$Y(x,t) = \frac{1}{2}\left(1-\frac{x}{h(t)}\right) \tag{87}$$

We also have

$$L(x,t) = L_0(t)\sqrt{1-\left(\frac{x}{h}\right)^2} \tag{88a}$$

$$\begin{aligned}\sqrt{2k(x,t)} &= \sqrt{2K_0(t)}\sqrt{1-\left(\frac{x}{h}\right)^2} \\ &= \frac{2}{C_L}\dot{L}_0(t)\sqrt{1-\left(\frac{x}{h}\right)^2}\end{aligned} \tag{88b}$$

where in Eq. (88b), we have utilized the L_0 equation. Substituting Eqs. (88) into Eq. (86) gives us

$$\dot{Y} = \frac{x\dot{h}}{2h^2} = \frac{2C_\mu}{C_L N_Y}\frac{L_0\dot{L}_0 x}{h^3} \tag{89}$$

Utilizing $L_0 = \beta h$ and $\dot{L}_0 = \beta\dot{h}$ gives

$$\dot{Y} = \frac{x\dot{h}}{2h^2} = \frac{2C_\mu\beta^2}{C_L N_Y}\frac{x\dot{h}}{h^2} = \frac{2C_\mu\left(\frac{C_L N_L}{2C_\mu}\right)}{C_L N_Y}\frac{x\dot{h}}{h^2} = \frac{N_L}{N_Y}\frac{x\dot{h}}{h^2} \tag{90}$$

Inspection reveals that this equation can only be satisfied if we have

$$N_Y = 2N_L \tag{91}$$

Self-Similarity of the Internal Energy Equation

Our conservation equation for internal energy in one dimension is given by:

$$\begin{aligned}\rho\frac{De}{Dt} =& p\frac{\partial u}{\partial x} + \frac{\partial}{\partial x}\left(\frac{\mu_t}{N_e}\frac{\partial e}{\partial x}\right) \\ &- C_B A(x) g\sqrt{2k} + C_D\frac{\rho(2k)^{3/2}}{L}\end{aligned} \tag{92}$$

Applying incompressibility and small Atwood number assumptions, this equation reduces to:

$$\frac{De}{Dt} = \frac{\partial}{\partial x}\left(\frac{C_\mu L\sqrt{2k}}{N_e}\frac{\partial e}{\partial x}\right) + C_D\frac{(2k)^{3/2}}{L} \tag{93}$$

We assume the self-similar solution takes the following form:

$$e(x,t) = e_0 + e_1 f(x,t) \tag{94}$$

After some algebra, we arrive at the reduced energy equation.

$$\begin{aligned}\left(\frac{e_1 C_L V_0}{L_0}\right)\left(\frac{x}{h}\right)^2 =& -\frac{N_L}{N_e}\left(\frac{e_1 C_L V_0}{L_0}\right)\left[1-3\left(\frac{x}{h}\right)^2\right] \\ &+ C_D\frac{V_0^3}{L_0}\left[1-\left(\frac{x}{h}\right)^2\right]\end{aligned} \tag{95}$$

As we have done previously, we require that the constant terms and x^2 terms go to zero simultaneously. This gives us two moment equations. We start by considering the zero moment equation:

$$-\frac{N_L}{N_e}\left(\frac{e_1 C_L V_0}{L_0}\right) + C_D\frac{V_0^3}{L_0} = 0 \qquad \text{(Zero Moment)}$$

which can be rearranged to give

$$C_D V_0^2 = \frac{e_1 C_L N_L}{N_e} \tag{96}$$

Utilizing the zero moment equation, we can then write the second moment equation:

$$\left(\frac{e_1 C_L V_0}{L_0}\right) = \frac{2N_L}{N_e}\left(\frac{e_1 C_L V_0}{L_0}\right) \qquad \text{(Second Moment)}$$

In order to satisfy the second moment equation, we therefore require

$$N_e = 2N_L \tag{97}$$

Compressibility Concerns

In order to obtain a constraint for the compressibility coefficient C_c, we estimate that the total mass of eddies in an RT mixing layer (ρL^3) is conserved under compression. Mathematically, this statement translates to the following:

$$\frac{D}{Dt}\left(\rho L^3\right) = 3L^2\rho\frac{DL}{Dt} + L^3\frac{D\rho}{Dt} = 0 \tag{98}$$

Recall the continuity equation in one dimension:

$$\frac{D\rho}{Dt} = -\rho\frac{\partial \tilde{u}}{\partial x} \tag{99}$$

Substituting Eq. (99) into Eq. (98) and rearranging yields:

$$\frac{1}{3}\rho L\frac{\partial \tilde{u}}{\partial x} = \rho\frac{DL}{Dt} \tag{100}$$

This result suggests that the compressibility coefficient in Eq. (42) should be given approximately by

$$C_c = \frac{1}{3} \tag{101}$$

Summary of Constraints

We now have a set of 13 unknowns (C_A, C_B, C_C, C_D, C_L, C_μ, N_L, N_k, N_Y, N_e, α_b, θ, and $\frac{E_K}{\Delta \mathrm{PE}}$) and 8 relational constraints. These constraints are summarized in table 4. Clearly, we require an additional five constraints to close the coefficient set. Firstly, let us take $\theta = 0.25$ based on linear electric motor experimental data [51], and let us take $\frac{E_K}{\Delta \mathrm{PE}} = 0.5$ based on previous experimental and numerical observations of RT mixing [52,48]. Note that these values are the same as those used by Dimonte and Tipton [20]. Where Dimonte and Tipton chose $\alpha_b = 0.060$, however, to be consistent with the majority of experimental data available at the time (which in general were observations of immiscible fluid mixing), here we choose $\alpha_b = 0.025$ to be consistent with the majority of simulation data of miscible fluid mixing [48]. To close out our constraints, it is desirable to enforce the Kolmogorov relationship between dissipation of turbulence kinetic energy and the turbulent length scale.

$$\varepsilon = C_D\frac{(2k)^{3/2}}{L} = \frac{k^{3/2}}{L} \tag{102}$$

Table 4 Relational Constraints

Constraint	Note
$C_A = \sqrt{\frac{2C_\mu}{C_L N_L}}$	Eq. (56)
$N_k = 2N_L$	Eq. (61)
$\frac{C_D}{C_L} = \frac{2-3\theta}{4\theta}$	Eq. (68)
$C_B = \frac{4\alpha_b\left(1+2\frac{C_D}{C_L}\right)}{\sqrt{\frac{C_\mu C_L}{N_K}}}$	Eq. (72)
$\frac{C_\mu C_L}{N_k} = 8\alpha_b\frac{\Delta \mathrm{PE}}{E_K}$	Eq. (84)
$N_Y = 2N_L$	Eq. (91)
$N_e = 2N_L$	Eq. (97)
$C_c = \frac{1}{3}$	Eq. (101)

Table 5 Additional Constraints

Constraint	Note
$\alpha_b = 0.025$	Ref. [48]
$\theta = 0.25$	Ref. [51]
$\frac{E_K}{\Delta \mathrm{PE}} = 0.5$	Ref. [52]
$C_D = \frac{1}{2\sqrt{2}}$	Eq. (103)
$C_\mu = \frac{0.288}{\sqrt{2}}$	Ref. [53]

Clearly, to enforce this relationship, we require:

$$C_D = \frac{1}{2\sqrt{2}} \approx 0.35 \tag{103}$$

Furthermore, we would like the new coefficient set to correctly capture Kelvin-Helmholtz instability; this requires $C_\mu << 1$. For our constraint on C_μ, let us take the value that is consistent with experimental measurements of RT mixing by Banerjee *et al* [53].

$$C_\mu = \frac{0.288}{\sqrt{2}} \approx 0.20 \tag{104}$$

We now have a complete set of 13 unknowns and 13 constraints, summarized in tables 4 and 5. Applying these constraints and translating into the notation used in Eqs. (13) through (18) gives us the complete coefficient set previously identified in table 1.

References

1. R. Richtmyer, Commun. Pure Appl. Math **8**, 297 (1960)
2. E. Meshkov, Sov. Fluid Dyn. **4**, 101 (1969)
3. M. Brouillette, Annu. Rev. Fluid Mech. **34**, 445 (2002)
4. A. Smits, J.P. Dussauge, *Turbulent Shear Layers in Supersonic Flow*, 2^{nd} edn. (Springer, New York, NY, 2006)
5. J. Lindl, R. McCrory, E. Campbell, Physics Today **45**, 32 (1992)
6. D. Arnett, Ap. J. Suppl. **127**, 213 (2000)
7. J. Yang, T. Kubota, E. Zukoski, AIAA J. **31**, 854 (1993)
8. B. Collins, J. Jacobs, J. Fluid Mech. **464**, 113 (2002)
9. J. Jacobs, J. Sheeley, Phys. Fluids **8**, 405 (1996)
10. M. Latini, O. Schilling, W. Don, J. Comput. Phys. **221**(2), 805 (2007)
11. J.F. Haas, B. Sturtevant, J. Fluid Mech. **181**, 41 (1987)
12. J. Jacobs, Phys. Fluids A **5**(9), 2239 (1993)
13. C. Tomkins, S. Kumar, G. Orlicz, K. Prestridge, J. Fluid Mech. **611**, 131 (2008)
14. S. Shankar, S. Kawai, S. Lele, Phys. Fluids **23**(024102) (2011)

15. J.S. Bai, L.Y. Zou, T. Wang, K. Liu, W.B. Huang, J.H. Liu, P. Li, D.W. Tan, C.L. Liu, Phys. Rev. E **82**(056318) (2010)
16. P. Li, J.S. Bai, T. Wang, L.Y. Zou, Sci China Phys. Mech. Astron. **53**(2), 262 (2010)
17. R. Moser, P. Moin, Direct numerical simulation of curved turbulent channel flow. Report TM-85974, NASA, Mountain View, CA (1984)
18. J. Kim, P. Moin, R. Moser, J. Fluid Mech. **177**, 133 (1987)
19. S. Pope, *Turbulent Flows*, 5th edn. (Cambridge University Press, 2008)
20. G. Dimonte, R. Tipton, Phys. Fluids **18**(085101) (2006)
21. A. Cook, Phys. Fluids **21**(055109) (2009)
22. J. Hirschfelder, C. Curtiss, R. Bird, *Molecular Theory of Gases and Liquids*, revised edn. (Wiley, New York, NY, 1964)
23. R. Reid, J. Pransuitz, B. Poling, *The Properties of Gases and Liquids* (McGraw Hill, New York, NY, 1987)
24. J. Ramshaw, J. Non-Equilib. Thermodyn. **15**, 295 (2009)
25. J. Waltz, T. Gianakon, Computer Physics Communications **183**, 70 (2012)
26. M. Brüggen, E. Scannapieco, S. Heinz, Mon. Not. R. Astron. Soc. **395**, 2210 (2009)
27. V. Smalyuk, O. Hurricane, J. Hansen, G. Langstaff, D. Martinez, H.S. Park, K. Raman, B. Remington, H. Robey, O. Schilling, R. Wallace, Y. Elbaz, A. Shimony, D. Shvarts, C.D. Stefano, R. Drake, D. Marion, C. Krauland, C. Kuranz, High Energy Density Physics **9**, 47 (2013)
28. R. Sharp, R. Barton, HEMP advection model. Report UCID 17809, Lawrence Livermore Laboratory, Livermore, CA (1981)
29. R. Darlington, T. McAbee, G. Rodrigue, Computer Physics Communications **135**, 58 (2001)
30. T. Kolev, R. Rieben, J. Comput. Phys. **228**, 8336 (2009)
31. M. Berger, J. Oliger, J. Comput. Phys. **53**, 484 (1984)
32. M. Berger, P. Colella, J. Comput. Phys. **82**, 64 (1989)
33. G. Boffetta, R. Ecke, Annu. Rev. Fluid Mech. **44**, 427 (2012)
34. J. Kent, J. Thuburn, N. Wood, Q. J. R. Meterol. Soc. **138**, 365 (2012)
35. G. Batchelor, Phys. Fluids Suppl. II **12**, 233 (1969)
36. V. Weirs, T. Dupont, T. Plewa, Phys. Fluids **20**(044102) (2008)
37. J. Boris, in *Whither turbulence? Turbulence at the Crossroads*, ed. by J. Lumley (Springer-Verlag, 1997), pp. 344–353
38. R. Darlington, T. McAbee, G. Rodrigue, Computer Physics Communications **144**, 261 (2002)
39. C. Fureby, F. Grinstein, AIAA J. **37**, 544 (1999)
40. L. Margolin, W. Rider, Int. J. Meth. Fluids **39**, 821 (2002)
41. P. Sagaut, *Large eddy simulation for incompressible flows*, 3rd edn. (Cambridge University Press, 2006)
42. F. Grinstein, L. Margolin, W. Rider, *Implicit Large Eddy Simulation*, 1st edn. (Cambridge University Press, 2007)
43. B. Johnson, O. Schilling, Journal of Turbulence **12**(36), 1 (2011)
44. B. Johnson, O. Schilling, Journal of Turbulence **12**(37), 1 (2011)
45. S. Kawai, S. Shankar, S. Lele, J. Comput. Phys. **229**, 1739 (2010)
46. B. Olson, J. Greenough, Phys. Fluids **26**, 101702 (2014)
47. G. Taylor, Proc. R. Soc. Lond. **A151**, 421 (1935)
48. G. Dimonte, D. Youngs, A. Dimits, S. Weber, M. Marinak, S. Wunsch, C. Garasi, A. Robinson, M. Andrews, P. Ramaprabhu, A. Calder, B. Fryxell, J. Biello, L. Dursi, P. MacNeice, K. Olson, P. ricker, R. Rosner, F. Timmes, H. Tufo, Y.N. Young, M. Zingale, Phys. Fluids **16**(5), 1668 (2004)
49. A. Banerjee, R. Gore, M. Andrews, Physical Review E **82**(4), 046309 (2010)
50. R. Tipton, G. Dimonte. Test problems for KL turbulent mix models. unpublished (2011)
51. G. Dimonte, M. Schneider, Phys. Fluids **12**(304) (2000)
52. P. Ramaprabhu, M. Andrews, J. Fluid Mech. **502**, 233 (2004)
53. A. Banerjee, W. Kraft, M. Andrews, J. Fluid Mech. **659**, 127 (2010)